

Similarity solutions and regularisation of inertial surfactant dynamics

Jun Eshima ¹, Luc Deike ^{1,2} and Howard A. Stone ¹

Corresponding authors: Howard A. Stone, hastone@princeton.edu; Luc Deike, ldeike@princeton.edu

(Received 14 July 2025; revised 20 September 2025; accepted 22 September 2025)

Surface tension gradients of air–liquid–air films play a key role in governing the dynamics of systems such as bubble caps, foams, bubble coalescence and soap films. Furthermore, for common fluids such as water, the flow due to surface tension gradients, i.e. Marangoni flow, is often inertial, due to the low viscosity and high velocities. In this paper, we consider the localised deposition of insoluble surfactants onto a thin air–liquid–air film, where the resulting flow is inertial. As observed by Chomaz (2001 *J. Fluid Mech.* 442, 387–409), the resulting governing equations with only inertia and Marangoni stress are similar to the compressible gas equations. Thus, shocks are expected to form. We derive similarity solutions associated with the development of such shocks, where the mathematical structure is closely related to the Burgers equation. It is shown that the nonlinearity of the surface tension isotherm has an effect on the strength of the shock. When regularisation mechanisms are included, the shock front can propagate and late-time similarity solutions are derived. The late-time similarity solution due to regularisation by capillary pressure alone was found by Eshima *et al.* (2025 *Phys. Rev. Lett.* 134, 214002). Here, the regularisation mechanism is generalised to include viscous extensional stress.

Key words: thin films, complex fluids, capillary flows

1. Introduction

1.1. Background

Surface tension gradients at liquid–air interfaces induce Marangoni flow (Manikantan & Squires 2020). Considering such a flow is important in understanding air–liquid–air films, such as those found on the film cap of surface bubbles, films in foam structures, films prior to bubble coalescence and soap films. In particular, the bursting of surface bubbles

¹Department of Mechanical and Aerospace Engineering, Princeton University, Princeton, NJ 08544, USA ²High Meadows Environmental Institute, Princeton University, Princeton, NJ 08544, USA

has been widely investigated due to their importance in the environment, such as the emission of sea spray aerosols, that affect the mass exchange between the atmosphere and the ocean (Veron 2015; Deike 2022), health (Bourouiba 2021) and industry. Consequently, understanding the details of why, when and how bubbles burst, along with the emitted aerosol size distribution, are of practical importance. Currently, localised surface tension variations on the bubble cap are thought of as the leading candidate for the rupture of the bubble cap (Néel & Villermaux 2018; Poulain, Villermaux & Bourouiba 2018), which is a curved air–liquid–air film. Models of thinning of air–liquid–air films due to surface tension variations have been investigated by various authors (Bowen & Tilley 2013; Kitavtsev, Fontelos & Eggers 2018; Néel & Villermaux 2018; Eshima *et al.* 2024, 2025).

In many applications of air-liquid-air films with liquids such as water, the relevant Marangoni flow is inertial (e.g. bubbles on the ocean). In this paper, we consider the model problem of the localised deposition of insoluble surfactants onto a thin air-liquid-air film, otherwise at rest. As observed by Chomaz (2001), the resulting governing equations accounting only for inertia and Marangoni effects, referred to as the IM regime in this paper, are closely related to the compressible gas equations upon identifying the surfactant concentration Γ with the (negative) gas pressure and the thickness of the film with the gas density. Consequently, finite-time shocks are expected to form, that is, a shock develops as $t \to t_*^-$ for some finite t_* . In this paper, we derive similarity solutions of such shock formation, where the local problem is seen to simplify effectively to the inviscid Burgers equation. It is found that the local nonlinearity of the surface tension σ dependence on the surfactant concentration Γ , given by $\sigma = \sigma(\Gamma)$, must be accounted for in determining the shock strength.

With the inclusion of regularisation mechanisms, the shock propagates. Eshima, Stone & Deike (2025) considered capillary stress as the sole regularisation mechanism and found the late-time inertia–Marangoni–capillary (IMC) similarity solution of the propagation. Here, the regularisation mechanism is generalised to include viscous extensional stress and late-time similarity solutions are found. In other words, we consider the inertia–Marangoni–capillary–extensional (IMCE), IMC (Eshima *et al.* 2025) and inertia–Marangoni–extensional (IME) regimes, where the acronym denotes which physics are in the dominant balance: inertia (I), Marangoni (M), capillary stress (C) and extensional stress (E). We derive late-time similarity solutions for the three distinct cases regimes using a single general approach and investigate the coherent relationship between the different regimes. In particular, it is shown that the IMC and IME regimes may be recovered from the IMCE regime in the appropriate limits.

1.2. Thin-film equations

Here, we give the governing thin-film equations considered in this study. Consider an axisymmetric incompressible Newtonian film with dynamic viscosity μ and density ρ . Let the radial direction be given by \hat{r} and the axial direction be given by \hat{z} . The top and bottom of the film are given, respectively, by $\hat{z} = \pm (1/2)\hat{h}(\hat{r},\hat{t})$ with the surfactant concentration on the top and bottom of the film given by $\hat{\Gamma}(\hat{r},\hat{t})$. Assume that the surface tension $\hat{\sigma} = \hat{\sigma}(\hat{\Gamma}(\hat{r},\hat{t}))$ depends only on the local surfactant concentration. In other words, we consider a top-bottom symmetric film. We also ignore the effect of the surrounding air (see figure 1). Let the radial velocity be given by \hat{u} . We consider the localised deposition of insoluble surfactants onto a film otherwise at rest with uniform thickness \hat{h}_i . The initial surfactant distribution is given by $\hat{\Gamma}_i(\hat{r})$ where $\hat{\Gamma}_i \to 0$ as $r \to \infty$.

The non-dimensionalisation below is given by Eshima *et al.* (2025). The characteristic surfactant concentration, horizontal length scale and surface tension deficit are given by

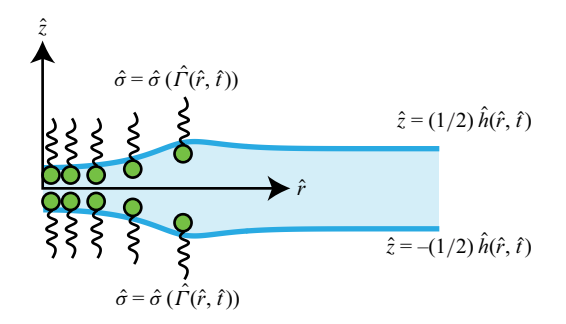


Figure 1. Schematic of a thin film with thickness $\hat{h}(\hat{r},\hat{t})$; the \hat{r} axis is in the radial direction, the \hat{z} axis is in the axial direction and \hat{t} is time. The top/bottom of the surface of the film is given by $\hat{z} = \pm (1/2)\hat{h}(\hat{r},\hat{t})$. The surfactant concentration at the top/bottom is given by $\hat{\Gamma}(\hat{r},\hat{t})$ and surface tension at the top/bottom of the film is given by $\hat{\sigma} = \hat{\sigma}(\hat{\Gamma}(\hat{r},\hat{t}))$.

$$(\hat{\Gamma}_m, \mathcal{L}, \Delta \Sigma) = \left(\max \hat{\Gamma}_i, \pi^{-\frac{1}{2}} \left(\frac{N_{\Gamma}}{\hat{\Gamma}_m} \right)^{\frac{1}{2}}, -\hat{\Gamma}_m \frac{d\hat{\sigma}}{d\hat{\Gamma}} \Big|_{\hat{\Gamma} = 0} \right), \tag{1.1}$$

where $N_{\Gamma} = 2\pi \int_0^\infty \hat{r} \hat{\Gamma} d\hat{r}$ is the total amount of surfactant, which is conserved. The particular convention of the constants in (1.1) is chosen so that the non-dimensional surfactant concentration, total amount of surfactant and surface tension, respectively satisfy max $\Gamma_i = 1$, $2\pi \int_0^\infty r \Gamma dr = \pi$ and $\sigma(\Gamma) = -\Gamma$ for $\Gamma \ll 1$, which simplifies the calculations presented in this paper. Then, the non-dimensionalisation for the thin-film equations is given by

$$(\hat{r}, \hat{t}, \hat{u}, \hat{h}, \hat{\Gamma}, \hat{\sigma}) = \left(\mathcal{L}r, \sqrt{\frac{\rho \epsilon \mathcal{L}^3}{\Delta \Sigma}} t, \sqrt{\frac{\Delta \Sigma}{\rho \epsilon \mathcal{L}}} u, \epsilon \mathcal{L}h, \hat{\Gamma}_m \Gamma, \Sigma + \Delta \Sigma \sigma \right), \tag{1.2}$$

where $\epsilon := \hat{h}_i/\mathcal{L}$ is the aspect ratio of the film, assumed small $\epsilon \ll 1$ and Σ is the constant value of the surface tension without surfactants. We consider the case where inertia and Marangoni stresses are in dominant balance and hence $\rho \hat{h}(\partial \hat{u}/\partial \hat{t}) \sim (\partial \hat{\sigma}/\partial \hat{r})$. We consider the time scale at which the film thins appreciably, and hence from the kinematic boundary conditions $(\partial \hat{h}/\partial \hat{t}) = -\hat{u}(\partial \hat{h}/\partial \hat{r}) + 2\hat{w}$ at $\hat{z} = \pm (1/2)\hat{h}$, where \hat{w} denotes the vertical velocity, we have $(\partial \hat{h}/\partial \hat{t}) \sim \epsilon \hat{u}$ since $\hat{w} \sim \epsilon \hat{u}$ from continuity. Then, the horizontal velocity scale is given by $\sqrt{\Delta \Sigma/(\rho \epsilon \mathcal{L})}$ and the time scale by $\sqrt{(\rho \epsilon \mathcal{L}^3)/(\Delta \Sigma)}$, as identified by Néel & Villermaux (2018).

The derivation of the thin-film equations is omitted since similar equations have already appeared in the literature (Erneux & Davis 1993; De Wit, Gallez & Christov 1994; Howell 1996; Breward 1999; Brenner & Gueyffier 1999; Chomaz 2001; Savva & Bush 2009; Eshima *et al.* 2024, 2025). In the limit of a thin film, $\epsilon \ll 1$, the Navier–Stokes equations give the one-dimensional thin-film equations. The leading-order radial velocity is one-dimensional, u = u(r, t), and the non-dimensional thin-film equations are given by

$$\frac{\partial u}{\partial t} + u \frac{\partial u}{\partial r} = \frac{2}{h} \frac{\partial \sigma}{\partial r} + \frac{1}{2\mathcal{M}} \frac{\partial}{\partial r} \left(\frac{1}{r} \frac{\partial}{\partial r} \left(r \frac{\partial h}{\partial r} \right) \right) + \frac{4}{Re} \frac{1}{h} \left(\frac{\partial}{\partial r} \left(\frac{h}{r} \frac{\partial}{\partial r} (ru) \right) - \frac{1}{2} \frac{u}{r} \frac{\partial h}{\partial r} \right), \tag{1.3a}$$

J. Eshima, L. Deike and H.A. Stone

$$\frac{\partial h}{\partial t} = -\frac{1}{r} \frac{\partial}{\partial r} (ruh), \tag{1.3b}$$

$$\frac{\partial \Gamma}{\partial t} = -\frac{1}{r} \frac{\partial}{\partial r} (r u \Gamma), \tag{1.3c}$$

where there are two non-dimensional parameters remaining

$$\mathcal{M} := \frac{\Delta \Sigma}{\epsilon^2 \Sigma}, \ Re := \sqrt{\frac{\rho \Delta \Sigma \mathcal{L}}{\epsilon \mu^2}}.$$
 (1.4)

Physically, \mathcal{M} is a Marangoni number that denotes the balance between Marangoni stress and capillary pressure gradient (Manikantan & Squires 2020). Similarly, the Reynolds number Re denotes the balance between inertia and viscous extensional stress. Note that Eshima $et\ al.\ (2025)$ used the notation $B=\mathcal{M}^{-1}$, as the focus was on the capillary waves, but the use of the notation \mathcal{M} is physically more helpful in discussing the transition between the different regimes in this paper. Another way to group the two parameters would be to consider an Ohnesorge number $Oh=\mu/\sqrt{\rho\Sigma\mathcal{L}}=Re^{-1}\sqrt{\epsilon\mathcal{M}}$, which has the benefit of being independent of the change in surface tension $\Delta\Sigma$.

It should be noted here that thin-film approaches are typically associated with viscously dominated flow (Oron, Davis & Bankoff 1997), such as for Marangoni flows of thin liquid films on a solid substrate (Jensen & Grotberg 1992). However for air-liquid-air films where the liquid is low viscosity, inertia plays an important role (Néel & Villermaux 2018). As an example, consider standard properties of water ($\rho \approx 10^3 \, \mathrm{kg \, m^{-3}}$, $\mu \approx 10^{-3} \, \mathrm{Pa \, s}$), an aspect ratio of $\epsilon = 0.1$ and a horizontal length scale $\mathcal{L} = 10^{-4} \, \mathrm{m}$ (typical length scale of inhomogeneities on soap films and bubble caps). Then, even a small surface tension variation such as $\Delta \Sigma = 10^{-4} \, \mathrm{N \, m^{-1}}$, which corresponds to a 0.1 % variation in the surface tension of water, would lead to $Re \approx 10$. For details of surfactant deposition on an air-liquid-air film in a viscous limit, see Eshima, Deike & Stone (2024).

The intuition for the thin-film equations is as follows. Equations (1.3a), (1.3b) and (1.3c) are balances of horizontal momentum, and conservation of mass and surfactant, respectively. Furthermore, the left-hand side of (1.3a) represents the inertia terms, while the three terms on the right-hand side of (1.3a) are the Marangoni stress, the capillary pressure gradient and the viscous extensional stress, respectively.

Taking far-field conditions as boundary conditions, the initial and boundary conditions are then given by

$$u = 0, \quad h = 1, \quad \Gamma = \Gamma_i(r) \text{ at } t = 0,$$
 (1.5)

and

$$u = 0, \quad h = 1, \quad \Gamma = 0 \text{ at } r = \infty.$$
 (1.6)

In this paper, for simplicity in the derivation, we assume an initial surfactant distribution $\Gamma_i(r)$ that decays faster than polynomials (e.g., a Gaussian distribution $\Gamma_i(r) = e^{-r^2}$). Assuming polynomial decay allows the same derivation (see § 3.5).

In this paper, we consider \mathcal{M} and Re greater than or equal to O(1) since we wish to consider the case where Marangoni and inertia terms are in the dominant balance. For the thin-film approach to be valid, we also require $Re \ll \epsilon^{-2}$ (Chomaz 2001). At $Re = O(\epsilon^{-2})$, the flow is no longer one-dimensional. When $\mathcal{M} = O(1)$, the capillary pressure gradient is in the dominant balance and when Re = O(1), viscous extensional stress is in the dominant balance. As a side note, it would not be physical to consider $\mathcal{M} \gg \epsilon^{-2}$, which would imply negative surface tension ($\Delta \Sigma \gg \Sigma$).

Then, there are four distinct regions in the parameter space, which are as follows: IM balance regime $(\mathcal{M} \gg 1, 1 \ll Re \ll \epsilon^{-2})$, IMC balance regime $(\mathcal{M} = O(1), 1 \ll Re \ll \epsilon^{-2})$, IME balance regime $(\mathcal{M} \gg 1, Re = O(1))$ and IMCE balance regime $(\mathcal{M} = O(1), Re = O(1))$. For a graphical summary, see figure 2.

1.3. *Outline of the paper*

The outline of the paper is as follows. In § 2, the similarity solutions for the inertial surfactant deposition problem without regularisation are given (IM regime). In §§ 3, 4, the inertial surfactant deposition problem with regularisation due to capillary stress and/or viscous extensional stress is given (IMCE, IMC and IME regimes). Finally, § 5 discusses the resolution of singularities that arise.

In this paper we present the derivation of the similarity solutions in their entirety. For the details of the numerical schemes used to solve the differential equations in the text, see the supplementary material. For a summary of the identified similarity solutions and the corresponding scalings, along with the final results of the derivations, see table 1.

2. Inertial surfactant deposition without regularisation: inertial-Marangoni regime

In this section, we consider the IM regime where the dominant balance in the horizontal component of momentum involves only inertia and Marangoni stresses. Then, the equation for u is given by

$$\frac{\partial u}{\partial t} + u \frac{\partial u}{\partial r} = \frac{2}{h} \frac{\partial \sigma}{\partial r},\tag{2.1}$$

and the equations for h and Γ are given by (1.3b) and (1.3c). In the case of a linear surface tension isotherm $\sigma(\Gamma) = -\Gamma$, Chomaz (2001) noted that (2.1), (1.3b) and (1.3c) are the compressible Euler equations upon identifying $-\Gamma$ with the pressure and h with the liquid density. It is then natural to expect shocks to form. We identify the similarity solution describing the shock formation and discuss the effect of nonlinear surface tension isotherms. In reality, the shock is regularised by the presence of other physical effects, such as capillary pressure and/or viscous extensional stress, as discussed later in the paper (see §§ 3, 4).

As a side note, since we consider a localised surfactant deposition, the characteristics of the differential equations should in general cross to form shocks, although we do not give a formal proof (cf. the condition for the inviscid Burgers equation $(\partial u/\partial t) + u(\partial u/\partial x) = 0$ to form a shock is that the initial condition $u(x, 0) = u_i(x)$ contains a point x_0 with $(\mathrm{d}u_i/\mathrm{d}x)|_{x=x_0} < 0$).

An example of the dynamics is given by the numerical solutions of the governing equations, as shown in figure 3, which illustrates the finite-time shock formation due to an initial Gaussian surfactant concentration $\Gamma_i(r) = e^{-r^2}$; the arrows in figure 3 depict the direction of increasing time. The panels in figure 3 show (a) surfactant concentration Γ , (b) thickness h and (c) horizontal velocity u. The colours for (b, c) correspond to the Marangoni stress $-(2/h)(\partial \Gamma/\partial r)$ (log scaled, values within $\pm 10^{-2}$ are set to be black) and the times shown in (a-c) are t=0,0.2,0.5,0.8,1.135. A finite-time shock singularity occurs (the derivatives become infinite) at $t\approx 1.136$, and hence the final time step shown t=1.135 is a time just before the shock singularity. Furthermore, to highlight the rapid variation in the neighbourhood of the shock, the insets to figure 3(a-c) show a magnified view at t=1.135 of the shock region. From the curves, it can be seen that, due to the non-uniform initial surfactant concentration Γ , there is a Marangoni flow away from r=0, which is strong enough to cause a finite-time shock to form. It may be noticed

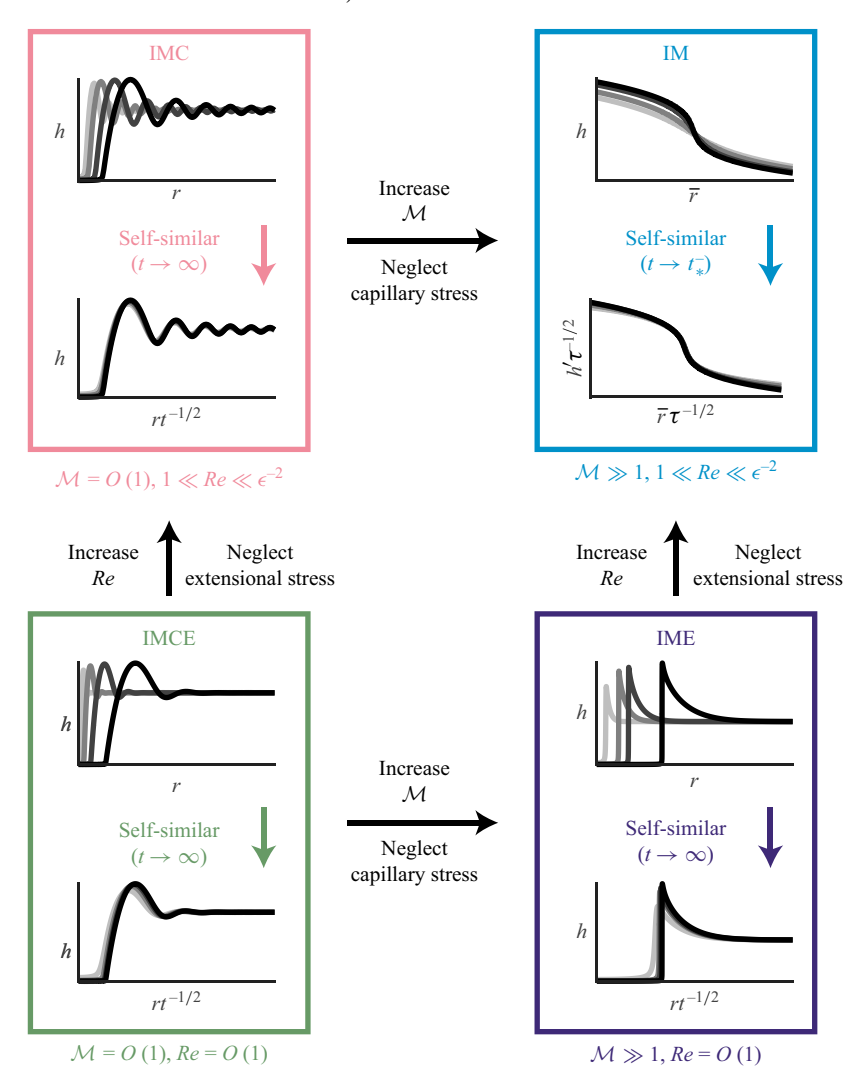


Figure 2. Summary of the parameter space considered in this paper, which investigates the thinning of an air-liquid-air film due to (insoluble) surfactant deposition. The axes are given by the two non-dimensional parameters, $\mathcal{M} = \Delta \Sigma/(\epsilon^2 \Sigma)$ and $Re = \sqrt{(\rho \Delta \Sigma \mathcal{L})/(\epsilon \mu^2)}$, where \mathcal{M} is a Marangoni number that denotes the balance between Marangoni stress and capillary pressure and the Reynolds number Re denotes the balance between inertia and the viscous extensional stress (see § 1.2 for details). The labels of the regions denote which physics are in dominant balance. The possible options are inertia (I), Marangoni (M), capillary stress (C) and extensional stress (E). Similarity solutions are identified in the four regimes. The system is assumed axisymmetric. The radial coordinate is given by r, time is given by t and the thickness of the liquid film is given by t and the thickness of the liquid film is given by t and the similarity solution $t \to t^-$, where a shock singularity occurs at some finite time t_* , is found in the IM regime (\bar{r} is the shock frame, t is the deviation from the value of t at the shock singularity t and t is the shock singularity. For the late-time similarity solutions, there is a front, and the asymptotic solution is found by matching between three regions: region I behind the front, region III ahead of the front and the transition region II. The temporal evolution is shown by colours (light grey to black as time increases).

Regime	Description and solution	Behaviour [as $t \to t_*^-$ for IM, $t \to \infty$ for IMC, IME, IMCE]
IM	Singular (finite time shock formation) shock formation similarity solution (2.19)	Shock region width $\sim (t_* - t)^{3/2}$ $u - u_*, h - h_*, \Gamma - \Gamma_* \sim (t_* - t)^{1/2}$ (()* denotes values at singularity)
IMC	Not singular late-time similarity solution Region I: (3.7) Region II: (3.13) Region III: (F3–F5)	$ \begin{aligned} &(u_{\rm I},h_{\rm I},\Gamma_{\rm I},\Delta r_{\rm I}) \sim (t^{-(1/2)},t^{-1},t^{-1},t^{1/2}) \\ &(\Delta u_{\rm II},h_{\rm II},\Gamma_{\rm II},\Delta r_{\rm II}) \sim (t^{-1},t^{-(1/2)},t^{-1},1) \\ &(u_{\rm III},h_{\rm III},\Delta r_{\rm III}) \sim (t^{-(1/2)},1,t^{1/2}),\Gamma_{\rm III} = 0 \end{aligned} $
IME	Singular (infinite time shock formation) late-time similarity solution Region I: (3.7) Region II: (3.17) Region III: (3.25, 3.26, 3.23)	$ \begin{aligned} &(u_{\rm I}, h_{\rm I}, \Gamma_{\rm I}, \Delta r_{\rm I}) \sim (t^{-(1/2)}, t^{-1}, t^{-1}, t^{1/2}) \\ &(\Delta u_{\rm II}, h_{\rm II}, \Gamma_{\rm II}, \Delta r_{\rm II}) \sim (t^{-(3/2)}, 1, t^{-1}, t^{-(1/2)}) \\ &(u_{\rm III}, h_{\rm III}, \Delta r_{\rm III}) \sim (t^{-(1/2)}, 1, t^{1/2}), \Gamma_{\rm III} = 0 \end{aligned} $
IMCE	Not singular late-time similarity solution Region I: (3.7) Region II: (3.13) Region III: (3.21–3.23)	$ \begin{aligned} &(u_{\rm I},h_{\rm I},\Gamma_{\rm I},\Delta r_{\rm I}) \sim (t^{-(1/2)},t^{-1},t^{-1},t^{1/2}) \\ &(\Delta u_{\rm II},h_{\rm II},\Gamma_{\rm II},\Delta r_{\rm II}) \sim (t^{-1},t^{-(1/2)},t^{-1},1) \\ &(u_{\rm III},h_{\rm III},\Delta r_{\rm III}) \sim (t^{-(1/2)},1,t^{1/2}),\Gamma_{\rm III} = 0 \end{aligned} $

Table 1. Summary of the similarity solutions in the four regimes (IM, IMC, IME, IMCE). As in the text, u is the velocity, h is the thickness, Γ is the surfactant, Δr is the spatial width and Δu is the velocity in the reference frame of the moving surfactant front $r = \eta_f t^{1/2}$ for constant η_f . For the IMC, IME and IMCE similarity solutions, the subscript Roman numerals refer to the three asymptotic regions identified in the text: region I is the region behind the moving front, region III is the region ahead of the moving front and region II is the transition region (see figure 2).

from figure 3 that the shock formation in the evolution of h and u look similar in shape to the case of shock formation arising from the inviscid Burgers equation (Pomeau *et al.* 2008; Eggers & Fontelos 2009). Indeed, the shock formation mechanism will be shown to be closely related to that of the inviscid Burgers equation and hence, for completeness, a brief review of the Burgers equation is given next in § 2.1.

2.1. Review: inviscid Burgers equation

In this subsection, we review the inviscid Burgers equation and the corresponding similarity solution associated with shock formation. The approach of Eggers & Fontelos (2009) is followed closely. The inviscid Burgers equation for velocity u = u(x, t) is given by

$$\frac{\partial u}{\partial t} + u \frac{\partial u}{\partial x} = 0, \tag{2.2}$$

where x denotes the spatial coordinate and t denotes time. Consider the formation of a shock at time t_* , occurring at $x = x_*$ with $u_* = u(x_*, t_*)$. The mechanism behind the shock formation can be described as follows. Close enough to the singularity in space and time, (2.2) is to leading order just a constant speed advection equation $(\partial u/\partial t) + u_*(\partial u/\partial x) = 0$, which on its own would not lead to shock formation. Instead, the next-order nonlinearity $(u - u_*)(\partial u/\partial x)$ gives rise to the shock formation.

It is convenient when there is formation of a front to perform analysis in the frame of the translating front. Then, in order to investigate the behaviour near the shock in space and time, the variables $u' := u - u_*$, $\overline{x} := x - x_* + u_*\tau$ and $\tau := t_* - t$ are considered.

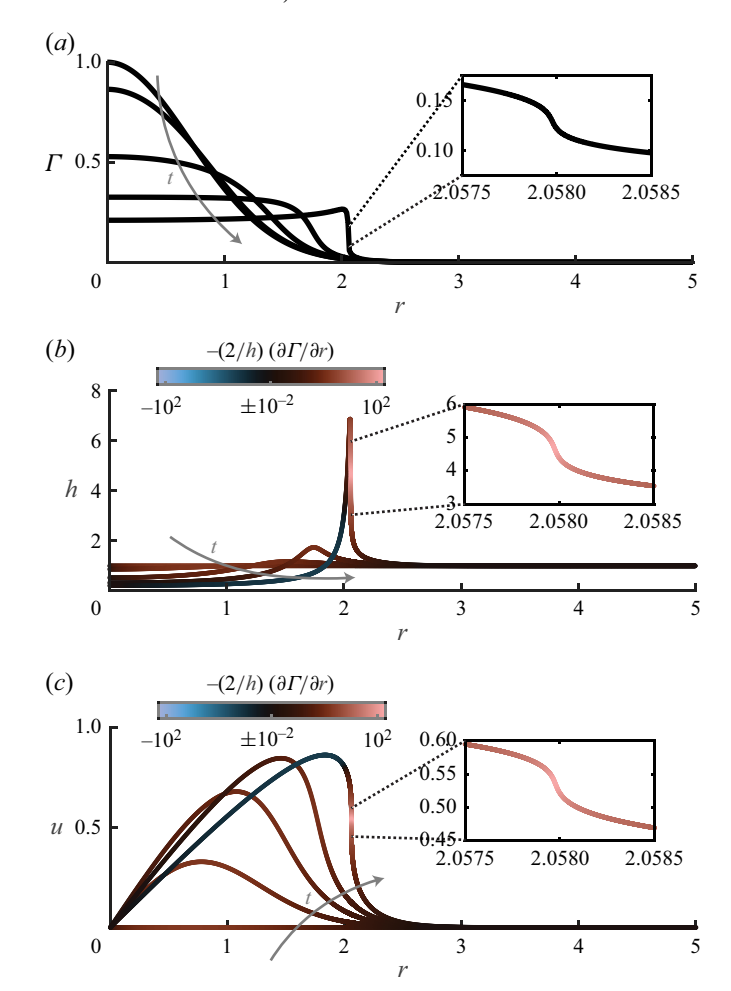


Figure 3. Example of shock formation with surface tension isotherm $\sigma(\Gamma) = -\Gamma$ and Gaussian initial surfactant distribution $\Gamma_i(r) = e^{-r^2}$. (a) Surfactant concentration Γ . (b) Thickness h. (c) Horizontal velocity u. In (b, c), the Marangoni stress $-(2/h)(\partial \Gamma/\partial r)$ gives the colour (Crameri 2021) of the curves (log scaled, values within $\pm 10^{-2}$ are set to be black). Times shown in (a-c) are t=0,0.2,0.5,0.8,1.135. A finite-time shock singularity occurs (the derivatives become infinite) at $t\approx 1.136$, and hence the final time step shown t=1.135 is a time just before the shock singularity. The insets to (a,b,c) show the magnified view of the solution at t=1.135. The arrows denote the direction of increasing time.

The definition of τ is chosen such that as $t \to t_*^-$, then $\tau \to 0^+$. Substitution of the definitions into (2.2) gives

$$\frac{\partial u'}{\partial \tau} - u' \frac{\partial u'}{\partial \overline{x}} = 0. \tag{2.3}$$

A local similarity solution of the shock as $\tau \to 0^+$ can be found by considering the self-similarity ansatz (Eggers & Fontelos 2009)

$$u' = \tau^{\alpha - 1} F(\xi), \tag{2.4}$$

where $\xi := \overline{x}\tau^{-\alpha}$ and the scaling comes from the balance between $\partial u'/\partial \tau$ and $u'(\partial u'/\partial \overline{x})$. Note that the constant $\alpha \geqslant 1$ (since u' does not blow up) cannot be deduced from scaling analysis alone and is deduced from stability considerations. In other words,

the self-similarity is of the second kind. Then, (2.3) and (2.4) give

$$(\alpha - 1)F - \alpha \xi \frac{\mathrm{d}F}{\mathrm{d}\xi} - F \frac{\mathrm{d}F}{\mathrm{d}\xi} = 0, \tag{2.5}$$

which can be integrated when $\alpha - 1 \neq 0$ to give

$$\xi = -F - KF^{\frac{\alpha}{\alpha - 1}},\tag{2.6}$$

for some constant K > 0; the case $\alpha = 1$ gives $F = -\xi$, which cannot be matched to the solution away from the singularity (Eggers & Fontelos 2009). There is then a discrete number of possible α given by the constraint of F being smooth everywhere $(\alpha/(\alpha-1)$ needs to be an odd integer). Out of the possible α , it can be shown that only $\alpha = 3/2$ gives a stable similarity solution (Eggers & Fontelos 2009). In summary, unravelling definitions, the similarity solution for the Burgers equation, (2.2), is given by

$$u = u_* + (t_* - t)^{\frac{1}{2}} F\left(\frac{x - x_* + u_*(t_* - t)}{(t_* - t)^{\frac{3}{2}}}\right),\tag{2.7}$$

where $\xi = -F - KF^3$ for some constant K > 0.

2.2. Derivation of the similarity solution in the IM regime

In this subsection, we give the derivation of the similarity solution associated with shock formation in the IM regime. Throughout the derivation, analogies to the Burgers equation are given (see § 2.1). Consider the formation of a shock at time t_* , occurring at $r = r_*$ with

$$(u_*, h_*, \Gamma_*) := (u(r_*, t_*), h(r_*, t_*), \Gamma(r_*, t_*)). \tag{2.8}$$

The singularity values $(u_*, h_*, \Gamma_*, r_*, t_*)$ are obtained numerically (see supplementary material) and are taken to be known. In order to investigate the behaviour near the shock, let

$$(u', h', \Gamma', r', \tau) := (u - u_*, h - h_*, \Gamma - \Gamma_*, r - r_*, t_* - t). \tag{2.9}$$

Then, (2.1), (1.3b) and (1.3c) give

$$\frac{\partial u'}{\partial \tau} - (u_* + u') \frac{\partial u'}{\partial r'} + \frac{2 \frac{\mathrm{d}\sigma}{\mathrm{d}\Gamma} (\Gamma_* + \Gamma')}{h_* + h'} \frac{\partial \Gamma'}{\partial r'} = 0, \tag{2.10a}$$

$$\frac{\partial h'}{\partial \tau} - (u_* + u') \frac{\partial h'}{\partial r'} - \frac{(h_* + h')(u_* + u')}{r_* + r'} - (h_* + h') \frac{\partial u'}{\partial r'} = 0, \tag{2.10b}$$

$$\frac{\partial \Gamma'}{\partial \tau} - (u_* + u') \frac{\partial \Gamma'}{\partial r'} - \frac{(\Gamma_* + \Gamma')(u_* + u')}{r_* + r'} - (\Gamma_* + \Gamma') \frac{\partial u'}{\partial r'} = 0. \tag{2.10c}$$

As $\tau \to 0^+$, the shock forms and hence the derivative terms become singular (e.g. $|\partial u'/\partial r'| \to \infty$). Then, finite terms such as h_*u_*/r_* are not leading-order terms. To leading order, as $\tau \to 0^+$, (2.10) simplifies to

$$\frac{\partial}{\partial \tau} \begin{bmatrix} u' \\ h' \\ \Gamma' \end{bmatrix} = \begin{bmatrix} u_* & 0 & \frac{V^2}{\Gamma_*} \\ h_* & u_* & 0 \\ \Gamma_* & 0 & u_* \end{bmatrix} \frac{\partial}{\partial r'} \begin{bmatrix} u' \\ h' \\ \Gamma' \end{bmatrix}, \tag{2.11}$$

where a velocity V is defined

$$V := \left(-\frac{2\frac{\mathrm{d}\sigma}{\mathrm{d}\Gamma}(\Gamma_*)\Gamma_*}{h_*} \right)^{\frac{1}{2}}.$$
 (2.12)

In this work, we only consider $(d\sigma/d\Gamma)|_{\Gamma=\Gamma_*} < 0$, as is physically relevant for surfactants, and hence V > 0. The leading-order Burgers equation (2.2) is an advection equation and consequently a change of coordinates is applied. Similarly, the leading-order matrix system (2.11) is simply a linear advection equation, where the matrix has eigenvalues $u_*, u_* +$ $V, u_* - V$ with corresponding eigenvectors $(0, 1, 0), (V, h_*, \Gamma_*), (V, -h_*, -\Gamma_*)$. Thus, in order to consider local shock formation, we change coordinates to be along a particular characteristic. The rest of this section considers shock formation along the $u_* + V$ characteristic, with space-time coordinates (\bar{r}, τ) , where $\bar{r} := r' + (u_* + V)\tau$. The u_* characteristic has an eigenvector that has a zero Γ component and is not considered. The similarity solution for the shock formation along the $u_* - V$ characteristic can be derived with an analogous method.

Now, we keep account of the order of magnitude of the terms appearing in (2.10)with respect to τ as $\tau \to 0^+$. As mentioned, to leading order, (2.10) is a linear advection equation and hence u', h', $\Gamma' = O(\tau^{\beta})$ for some constant β . Consequently, like the Burgers equation, the nonlinearity gives rise to the singularity and hence there is a balance $(\partial u'/\partial \tau) \sim u'(\partial u'/\partial \overline{r})$. Then, letting $\overline{r} = O(\tau^{\alpha})$ for the characteristic width of the shock region, $\beta = \alpha - 1$. Thus, from the leading-order expansion (2.11), since the $u_* + V$ characteristic has eigenvector (V, h_*, Γ_*) , we may write

$$u' = V(A(\overline{r}, \tau) + q_1 \tau^{\alpha - 1} + f_1(\overline{r}, \tau)),$$
 (2.13a)

$$h' = h_*(A(\overline{r}, \tau) + q_2 \tau^{\alpha - 1} + f_2(\overline{r}, \tau)),$$
 (2.13b)

$$\Gamma' = \Gamma_*(A(\overline{r}, \tau) + q_3 \tau^{\alpha - 1} + f_3(\overline{r}, \tau)), \tag{2.13c}$$

(2.14c)

where $A = O(\tau^{\alpha - 1})$ and f_1 , f_2 , f_3 are correction terms much smaller than $O(\tau^{\alpha - 1})$ and q_1, q_2, q_3 are constants. Since A is a function to be found, without loss of generality, $q_3 = -q_1$ (the explicit change of variables would be $(\tilde{A}, \tilde{q}_i) = (A + ((q_1 + q_3)/2)\tau^{\alpha - 1},$ $q_i - (q_1 + q_3)/2$) for i = 1, 2, 3). Then, substituting (2.13), correct to $O(\tau^{\alpha-2})$, into (2.10) gives (see Appendix A)

$$V\frac{\partial(A+q_{1}\tau^{\alpha-1})}{\partial\tau} + V^{2}\left(q_{2} - q_{1} - \frac{2\frac{d^{2}\sigma}{d\Gamma^{2}}(\Gamma_{*})\Gamma_{*}^{2}}{h_{*}V^{2}}q_{1}\right)\tau^{\alpha-1}\frac{\partial A}{\partial\overline{r}} + \frac{2\frac{d^{2}\sigma}{d\Gamma^{2}}(\Gamma_{*})\Gamma_{*}^{2}}{h_{*}}A\frac{\partial A}{\partial\overline{r}} + V^{2}\left(\frac{\partial f_{1}}{\partial\overline{r}} - \frac{\partial f_{3}}{\partial\overline{r}}\right) = 0, \qquad (2.14a)$$

$$h_{*}\frac{\partial(A+q_{2}\tau^{\alpha-1})}{\partial\tau} - Vh_{*}(q_{1}+q_{2})\tau^{\alpha-1}\frac{\partial A}{\partial\overline{r}} - 2h_{*}VA\frac{\partial A}{\partial\overline{r}} + Vh_{*}\left(\frac{\partial f_{2}}{\partial\overline{r}} - \frac{\partial f_{1}}{\partial\overline{r}}\right) = 0, \qquad (2.14b)$$

$$\Gamma_{*}\frac{\partial(A-q_{1}\tau^{\alpha-1})}{\partial\tau} - 2\Gamma_{*}VA\frac{\partial A}{\partial\overline{r}} + V\Gamma_{*}\left(\frac{\partial f_{3}}{\partial\overline{r}} - \frac{\partial f_{1}}{\partial\overline{r}}\right) = 0. \qquad (2.14c)$$

Rearranging and combining (2.14a) and (2.14c) gives

$$\frac{\partial A}{\partial \tau} + \frac{V}{2} \left(q_2 - q_1 - \frac{2 \frac{\mathrm{d}^2 \sigma}{\mathrm{d} \Gamma^2} (\Gamma_*) \Gamma_*^2}{h_* V^2} q_1 \right) \tau^{\alpha - 1} \frac{\partial A}{\partial \overline{r}} - V \left(1 - \frac{\frac{\mathrm{d}^2 \sigma}{\mathrm{d} \Gamma^2} (\Gamma_*) \Gamma_*^2}{h_* V^2} \right) A \frac{\partial A}{\partial \overline{r}} = 0, \tag{2.15}$$

which upon a change of variables

$$\overline{r}_{s} := \frac{\overline{r} - \frac{V}{2} \left(q_{2} - q_{1} - \frac{2 \frac{d^{2} \sigma}{d \Gamma^{2}} (\Gamma_{*}) \Gamma_{*}^{2}}{h_{*} V^{2}} q_{1} \right) \alpha^{-1} \tau^{\alpha}}{V \left(1 - \frac{\frac{d^{2} \sigma}{d \Gamma^{2}} (\Gamma_{*}) \Gamma_{*}^{2}}{h_{*} V^{2}} \right)},$$
(2.16)

gives

$$\frac{\partial A}{\partial \tau} - A \frac{\partial A}{\partial \overline{r}_s} = 0. \tag{2.17}$$

Therefore, we have arrived at precisely the inviscid Burgers (2.3). Physically, \overline{r}_s is the spatial coordinate in the frame of the moving shock. As per § 2.1, $\alpha = 3/2$ and A has a similarity solution given by $A = \tau^{(1/2)} F(\eta)$, where $\eta := \overline{r}_s \tau^{-(3/2)}$ and

$$\eta = -F - KF^3, \tag{2.18}$$

for some constant K > 0. Furthermore, by ensuring that the similarity solution may be matched to the outer region away from the local singularity region, it is possible to deduce that $q_1 = q_2 = 0$ (see Appendix B).

Then, unravelling all the definitions, the similarity solutions for the finite-time singularity for shock formation along the $u_* + V$ characteristic (see Appendix C for $u_* - V$ case) are given by

$$u = u_* + V(t_* - t)^{\frac{1}{2}} F\left(\frac{r - r_* + (u_* + V)(t_* - t)}{\left(1 - \frac{\frac{d^2 \sigma}{dr^2}(\Gamma_*)\Gamma_*^2}{h_* V^2}\right) V(t_* - t)^{\frac{3}{2}}}\right),$$
(2.19a)

$$h = h_* + h_*(t_* - t)^{\frac{1}{2}} F\left(\frac{r - r_* + (u_* + V)(t_* - t)}{\left(1 - \frac{\frac{d^2 \sigma}{d\Gamma^2}(\Gamma_*)\Gamma_*^2}{h_* V^2}\right) V(t_* - t)^{\frac{3}{2}}}\right), \tag{2.19b}$$

$$\Gamma = \Gamma_* + \Gamma_*(t_* - t)^{\frac{1}{2}} F\left(\frac{r - r_* + (u_* + V)(t_* - t)}{\left(1 - \frac{\frac{d^2 \sigma}{d\Gamma^2}(\Gamma_*)\Gamma_*^2}{h_* V^2}\right) V(t_* - t)^{\frac{3}{2}}}\right), \tag{2.19c}$$

where F is given by (2.18). Corrections are $O(t_* - t)$ as the shock forms with $t \to t_*^-$. In summary, like the Burgers equation, the shock region has width $O((t_* - t)^{3/2})$ and $u - u_*$, $h - h_*$, $\Gamma - \Gamma_* = O((t_* - t)^{1/2})$ in the shock as $t \to t_*^-$.

The method of translating coordinates along eigenvectors and reducing to Burgers equation, as shown above, is generalisable to a wider class of hyperbolic coupled partial differential equations and will be the subject of a future manuscript.

The details of shock formation may now be discussed. From (2.18), we have that $dF/d\eta = -(1+3KF^2)^{-1}$ and hence

$$\max \left| \frac{\mathrm{d}F}{\mathrm{d}\eta} \right| = 1,\tag{2.20}$$

which in turn gives that

$$\max \left| \frac{\partial u}{\partial r} \right| = \left(1 - \frac{\frac{\mathrm{d}^2 \sigma}{\mathrm{d} \Gamma^2} (\Gamma_*) \Gamma_*^2}{h_* V^2} \right)^{-1} (t_* - t)^{-1} \text{ as } t \to t_*^-, \tag{2.21}$$

where such an expression is useful for verification (see § 2.3) since (2.21) does not contain any undetermined coefficients (recall that the singularity values such as Γ_* are known numerically). Additionally, (2.21) shows that the nonlinearity of the surface tension isotherm has an effect on the shock formation. More precisely, if the surface tension isotherm is locally concave $(d^2\sigma/d\Gamma^2)|_{\Gamma=\Gamma_*} < 0$, then the shock is weakened, and if the surface tension isotherm is locally convex $(d^2\sigma/d\Gamma^2)|_{\Gamma=\Gamma_*} > 0$, the shock is strengthened.

Another useful expression, to be used in § 2.3 below for the purpose of additional numerical verification, is that

$$\max \left| \frac{\partial^2 u}{\partial r^2} \right| = \frac{25\sqrt{15}}{108} K^{\frac{1}{2}} V^{-1} \left(1 - \frac{\frac{d^2 \sigma}{d\Gamma^2} (\Gamma_*) \Gamma_*^2}{h_* V^2} \right)^{-2} (t_* - t)^{-\frac{5}{2}} \text{ as } t \to t_*^-, \quad (2.22)$$

since max $|d^2F/d\eta^2| = (25\sqrt{15}/108)K^{1/2}$ from (2.18). Equation (2.22) is also used to obtain an estimate for the constant K.

2.3. Verification of the similarity solution

In this subsection, we verify the similarity solution given by (2.19). In particular, a linear isotherm $\sigma(\Gamma) = -\Gamma$ with initial surfactant distribution $\Gamma_i(r) = e^{-r^2}$ is considered.

Since it is the derivatives $(\partial u/\partial r, \partial h/\partial r, \partial \Gamma/\partial r)$ that become singular, rather than the variables (u, h, Γ) themselves, the collapse to the similarity solution is harder to deduce systematically from seeing the profiles of u, h and Γ alone. Instead, we may verify the similarity solution using log-log plots to find the exponents. Since we wish to show two power-law behaviours, $u - u_* \sim (t_* - t)^{1/2}$ and $\overline{r} = r - r_* + (u_* + V)(t_* - t) \sim (t_* - t)^{3/2}$, it is sufficient to check the two predictions (2.21) and (2.22). In figure 4(a) we plot max $|\partial u/\partial r|$ versus $t_* - t$ and in figure 4(b) max $|\partial^2 u/\partial r^2|$ versus $t_* - t$ is reported. Numerical solutions of the thin-film equations are shown by solid curves and analytical similarity predictions (2.21) and (2.22) are shown by dashed lines. There are no fitting parameters in figure 4(a). In figure 4(b), $K \approx 0.083$ is chosen as the best fit, which gives an estimate for K for the example shown. Figure 4 shows that, indeed, $(\partial u/\partial r) \sim (t_* - t)^{-1}$ and $(\partial^2 u/\partial r^2) \sim (t_* - t)^{-(5/2)}$. The agreement breaks down at around $t_* - t \approx 5 \times 10^{-4}$ due to numerical inaccuracies, arising from issues such as not knowing t_* analytically (see supplementary material). This is a standard feature of log-log plots verifying numerical similarity solutions (Eggers & Fontelos 2015).

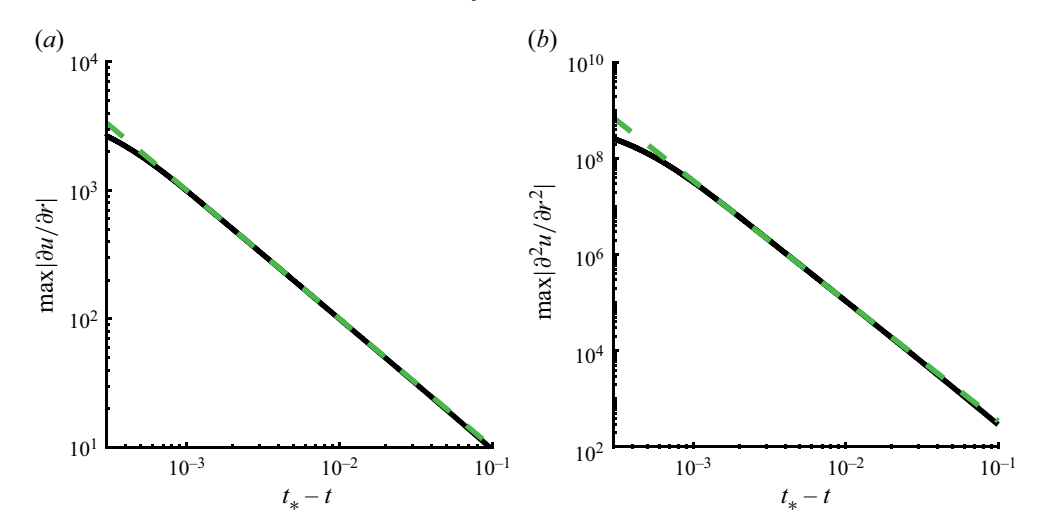


Figure 4. Systematic verification of the similarity solution for an example with a linear isotherm $\sigma(\Gamma) = -\Gamma$ and initial surfactant distribution $\Gamma_i(r) = e^{-r^2}$. The solid curves are the numerical solutions of the IM thin-film equations and the dashed lines are the similarity solution predictions (2.21, 2.22). (a) Log-log plot of max $|\partial u/\partial r|$ (no fitting parameters). (b) Log-log plot of max $|\partial^2 u/\partial r^2|$, where $K \approx 0.083$ is chosen as the best fit for the similarity solution prediction (2.22).

The collapse of the profiles for u, h and Γ is shown in figure 5, where the solid curves plotted have colours corresponding to $-\log(t_*-t)$. Figure 5(a) shows the horizontal velocity u evolving over time, where the spatial coordinate is given by $\overline{r} = r - r_* + (u_* + V)(t_* - t)$. Figure 5(b) shows the rescaled horizonal velocity $(u - u_*)V^{-1}(t_* - t)^{-(1/2)}$ versus the rescaled spatial coordinate $\overline{r}V^{-1}(t_*-t)^{-(3/2)}$, which is the expected similarity coordinate as predicted by (2.19a). Similarly, figure 5(c,e) shows the variables h and Γ and figure 5(d,f) displays the rescaled thickness and surfactant concentration versus the rescaled spatial coordinate. The dashed curve in figure 5(b,d,f) is $x = -y - Ky^3$ (where the horizontal axis is x and vertical axis is y). The coefficient $K \approx 0.083$ is that estimated from max $|\partial^2 u/\partial r^2|$ in figure 4(b), as above. We see in figure 5(b,d,f), respectively, that the dependent variables u, h and Γ collapse as $t \to t_*$, in good agreement with (2.19). With a more accurate numerical procedure, one could take smaller $t_* - t$ and also know u_* , h_* , Γ_* , r_* , t_* more accurately (see supplementary material).

2.4. Nonlinear effects of the surface tension isotherm

Here, some details of two examples with nonlinear effects of the surface tension isotherm are discussed. The first example is the Langmuir isotherm, $\sigma_{concave}(\Gamma) = \Gamma_{\infty} \log(1-(\Gamma/\Gamma_{\infty}))$ with $\Gamma_{\infty}=1.1$, corresponding to a concave isotherm. The prefactor of $\sigma_{concave}(\Gamma)$ is chosen so that $(\mathrm{d}\sigma_{concave}/\mathrm{d}\Gamma)|_{\Gamma=0}=-1$, which is how the problem was non-dimensionalised (see 1.2) and the choice of $\Gamma_{\infty}=1.1$ is so that the effects of concavity can be seen clearly. The second example is convex, $\sigma_{convex}(\Gamma)=-\Gamma_0 \tanh(\Gamma/\Gamma_0)$ with $\Gamma_0=0.1$. Again, the prefactor is chosen so that $(\mathrm{d}\sigma_{convex}/\mathrm{d}\Gamma)|_{\Gamma=0}=-1$ and the choice $\Gamma_0=0.1$ is so that the effects of convexity can be seen clearly.

A log-log plot of max $|\partial u/\partial r|$ as $t \to t_*^-$ for the two isotherms $\sigma_{concave}$ (blue) and σ_{convex} (pink) is presented in figure 6. Recall that the thin-film equations (solid curves) solved are given by (2.1), (1.3b) and (1.3c) and the similarity solution prediction (dashed

J. Eshima, L. Deike and H.A. Stone

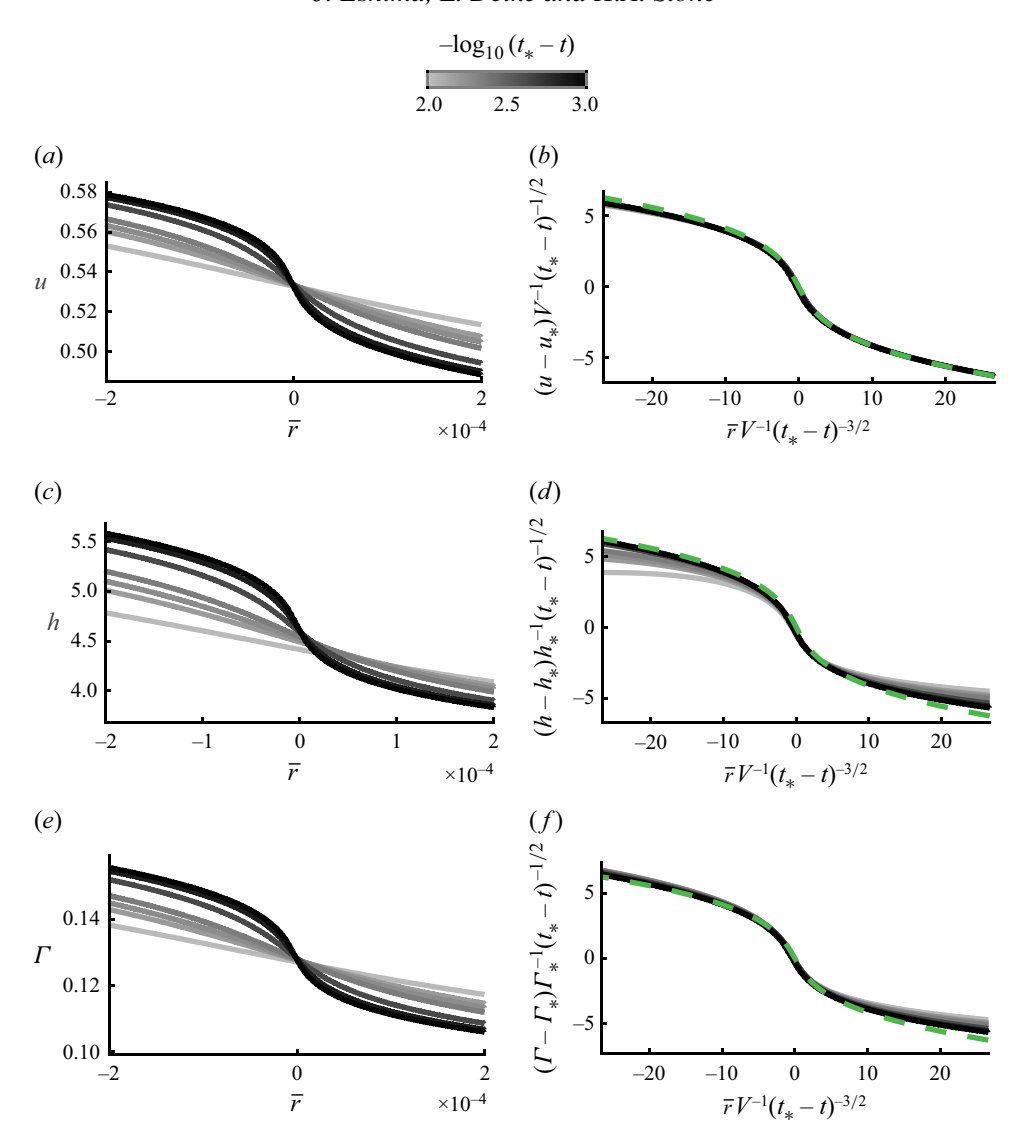


Figure 5. Shock formation with isotherm $\sigma(\Gamma) = -\Gamma$ and initial surfactant distribution $\Gamma_i(r) = e^{-r^2}$. A finite-time shock forms at $t = t_*$ (≈ 1.136). Colour bar: the solid curves have colour according to $-\log(t_* - t)$. (a) The horizontal velocity u with the spatial coordinate given by $\overline{r} = r - r_* + (u_* + V)(t_* - t)$, which is the coordinate system moving with the inflection point. (b) The appropriately rescaled horizontal velocity versus the appropriately rescaled spatial coordinate (i.e. the similarity solution). (c,d,e,f) Analogous to (a-b) but for thickness h and surfactant concentration Γ . The dashed curves in (b), (d) and (f) are the curve $x = -y - Ky^3$ where the horizontal axis is x, the vertical axis is y and $K \approx 0.083$ is a constant numerically estimated using relation (2.22) and figure 4(b).

lines) for $\max |\partial u/\partial r|$ is given by (2.21). The results shown in figure 6 demonstrate that, indeed, the similarity solution (2.21) accurately captures the nonlinear effects of the surface tension isotherm. The prediction $\max |\partial u/\partial r| = (t_* - t)^{-1}$ (black dashed) is the prediction for a locally linear isotherm $((d^2\sigma/d\Gamma^2)_{\Gamma=\Gamma_*}=0)$ and so we can see from figure 6 that, as expected, local concavity $(d^2\sigma/d\Gamma^2)_{\Gamma=\Gamma_*}<0$ weakens the shock and

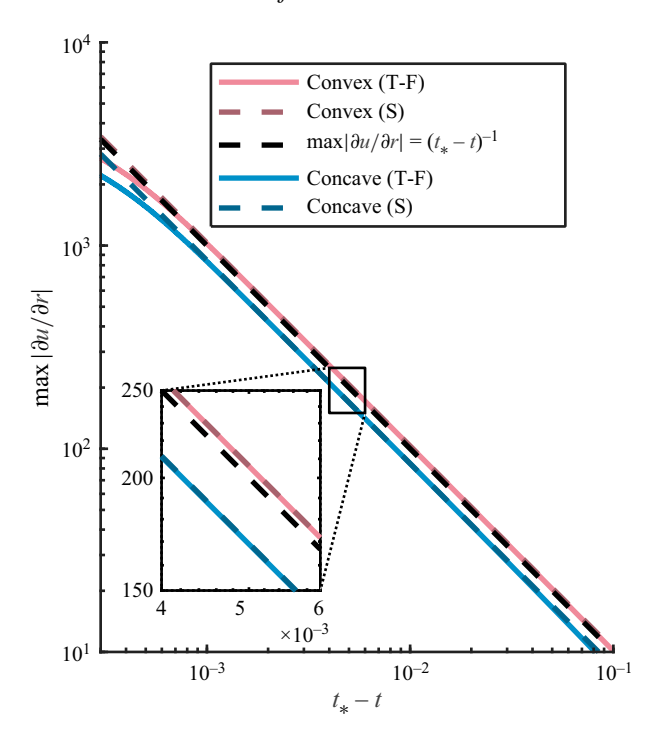


Figure 6. Effects of the nonlinearity of surface tension isotherms. Log-log plot of max $|\partial u/\partial r|$ as predicted by solution of the thin-film (T-F) equations (2.1), (1.3b), (1.3c) for an example concave isotherm as described in the text (blue solid). Analogous to an example convex isotherm as described in the text (pink solid). Initial surfactant distribution is $\Gamma_i = e^{-r^2}$. Corresponding similarity solution (S) predictions (2.21) are shown in dashed lines for the concave (blue dashed) and convex (pink dashed) cases. For comparison, the line max $|\partial u/\partial r| = (t_* - t)^{-1}$ is shown also (black dashed). Inset: magnified view of the same log-log plots.

local convexity $(d^2\sigma/d\Gamma^2)_{\Gamma=\Gamma_*}>0$ strengthens the shock, by changing the prefactor of the blow up of max $|\partial u/\partial r|$ as $t\to t_*^-$.

For the initial surfactant deposition $\Gamma_i = e^{-r^2}$ considered in this section, the effects of the change of $\max |\partial u/\partial r|$ are moderate. For the concave example discussed, $\max |\partial u/\partial r| \approx 0.85(t_*-t)^{-1}$ as $t\to t_*$, i.e. only a 15% decrease of the shock strength, which is due to the term $(\mathrm{d}^2\sigma/\mathrm{d}\Gamma^2)|_{\Gamma=\Gamma_*}\Gamma_*^2/(h_*V^2)$ being small in magnitude in (2.21). For the convex example discussed, $\max |\partial u/\partial r| \approx 1.03(t_*-t)^{-1}$ as $t\to t_*$. Different initial surfactant deposition profiles Γ_i may give stronger effects. In particular, it might be mathematically interesting to consider what would happen if $(\mathrm{d}^2\sigma/\mathrm{d}\Gamma^2)|_{\Gamma=\Gamma_*}\Gamma_*^2/(h_*V^2)=1$, where the derivation given in § 2.2 would have to be amended to account for higher-order terms, since the nonlinear term in (2.15) would vanish.

3. Inertial surfactant deposition with regularisation: derivation of the late-time similarity solution

When shock regularisation occurs, the shocks may propagate. Next, we consider two regularisation mechanisms for the surfactant deposition problem, namely capillary stress and viscous extensional stress. The three possible combinations of including or excluding these mechanisms (IMCE, IMC and IME regimes) allow for late-time similarity solutions

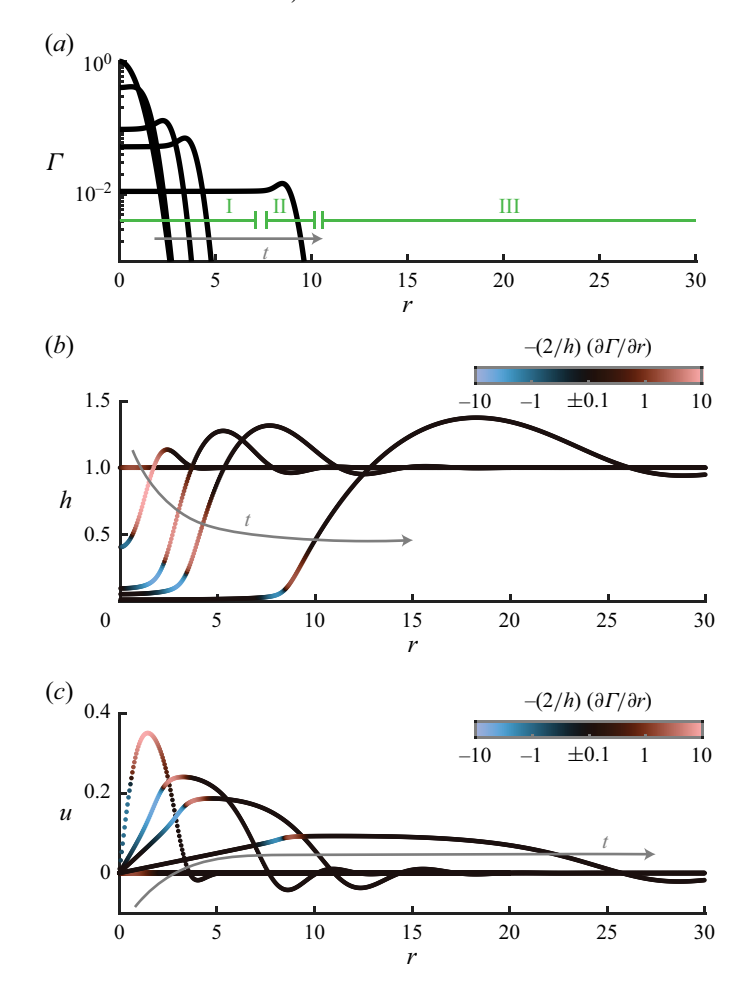


Figure 7. Sample evolution due to surfactant deposition for the IMCE (1.3) with $\sigma(\Gamma) = -\Gamma$, $\Gamma_i = e^{-r^2}$, $\mathcal{M} = 1$, Re = 10. The horizontal axes are given by the radial coordinate r. (a) Surfactant concentration Γ . (b) Thickness h. (c) Horizontal velocity u. Times shown are t = 0, 1, 5, 10, 50, where the arrows denote increasing time. The Marangoni stress $-(2/h)(\partial \Gamma/\partial r)$ gives the colour (Crameri 2021) of the curves (log scaled, values within ± 0.1 are set to be black). At late times, it can be seen that there are three regions: region I with a spatially uniform surfactant concentration, region III without surfactants and a transition region II that regularises the surfactant front. The figure is the analogue of figure 2 in (Eshima $et\ al.\ 2025$), but using the IMCE equations rather than the IMC (3.2, 1.3h, 1.3c).

of the surfactant front propagation. Since only late-time behaviour is considered, without loss of generality, $\sigma(\Gamma) = -\Gamma$ as $\Gamma \ll 1$ everywhere at late times (since the surfactant spreads and hence $\sigma(\Gamma) \approx (\mathrm{d}\sigma/\mathrm{d}\Gamma)|_{\Gamma=0}\Gamma = -\Gamma$).

The solution of the thin-film equation, (1.3), with $\mathcal{M} = 1$, Re = 10 and $\Gamma_i(r) = e^{-r^2}$ is reported in figure 7. At late times $t \gg 1$, there are three distinct regions: region I has a spatially uniform surfactant distribution (i.e. the Marangoni stress has vanished), region II is a transition region (i.e. regularisation) and region III has no surfactants.

For the IMC regime, where capillary stress is the sole regularisation mechanism, the late-time similarity solutions were identified by Eshima *et al.* (2025) through asymptotic matching between the three regions, where region II is the inner region where regularisation occurs and regions I and III are the outer regions to be matched. In this

paper, we find that this method may be generalised, with key differences in region II, where regularisation occurs.

In this section we derive the late-time similarity solution for inertial surfactant deposition in the IMCE regime, where both capillary stress and extensional stress appear in the dominant balance. The IME and IMC regimes may be identified as limits of the IMCE regime. In § 3.1, we present the outer regime scalings and in §§ 3.2, 3.3 and 3.4, respectively, the solutions in regions I, II and III are derived.

Henceforth, we will refer to the IMCE regime equations, corresponding to $\mathcal{M} = O(1)$ and Re = O(1), as conservation of mass (1.3b) and surfactant (1.3c), with conservation of momentum given by

$$\frac{\partial u}{\partial t} + u \frac{\partial u}{\partial r} = -\frac{2}{h} \frac{\partial \Gamma}{\partial r} + \frac{1}{2\mathcal{M}} \frac{\partial}{\partial r} \left(\frac{1}{r} \frac{\partial}{\partial r} \left(r \frac{\partial h}{\partial r} \right) \right) + \frac{4}{Re} \frac{1}{h} \left(\frac{\partial}{\partial r} \left(\frac{h}{r} \frac{\partial}{\partial r} (ru) \right) - \frac{1}{2} \frac{u}{r} \frac{\partial h}{\partial r} \right).$$
(3.1)

The IMC regime equations, corresponding to $\mathcal{M} = O(1)$ and $1 \ll Re \ll \epsilon^{-2}$, are given by conservation of mass (1.3b) and surfactant (1.3c), with conservation of momentum given by

$$\frac{\partial u}{\partial t} + u \frac{\partial u}{\partial r} = -\frac{2}{h} \frac{\partial \Gamma}{\partial r} + \frac{1}{2\mathcal{M}} \frac{\partial}{\partial r} \left(\frac{1}{r} \frac{\partial}{\partial r} \left(r \frac{\partial h}{\partial r} \right) \right). \tag{3.2}$$

The IME regime equations, corresponding to $\mathcal{M} \gg 1$ and Re = O(1), are given by conservation of mass (1.3b) and surfactant (1.3c), with conservation of momentum given by

$$\frac{\partial u}{\partial t} + u \frac{\partial u}{\partial r} = -\frac{2}{h} \frac{\partial \Gamma}{\partial r} + \frac{4}{Re} \frac{1}{h} \left(\frac{\partial}{\partial r} \left(\frac{h}{r} \frac{\partial}{\partial r} (ru) \right) - \frac{1}{2} \frac{u}{r} \frac{\partial h}{\partial r} \right). \tag{3.3}$$

The scaling for the outer regions is the same for the IMCE, IMC and IME regimes and may be derived as follows. Subscripts are used to denote the region under discussion. Let Δr denote the characteristic width of a given region. In region III, balancing inertia with the capillary stress gradient and/or viscous extensional stress, $u_{\rm III}t^{-1} \sim h_{\rm III}(\Delta r_{\rm III})^{-3}$ and/or $u_{\rm III}(\Delta r_{\rm III})^{-2}$. Additionally, considering conservation of mass, and far-field matching, $h_{\rm III} \rightarrow 1$, gives that $u_{\rm III} \sim t^{-(1/2)}$, $h_{\rm III} \sim 1$, $\Delta r_{\rm III} \sim t^{1/2}$. Integrating across region II, where there is a quasi-static balance between Marangoni, capillary and/or extensional stress (analogous to Rankine–Hugoniot jump conditions), one deduces that $\Gamma_I \sim h_{\rm III}^2 (\Delta r_{\rm III})^{-2}$ and/or $h_{\rm III}u_{\rm III}(\Delta r_{\rm III})^{-1}$, which implies that $\Gamma_I \sim t^{-1}$. Since $\int_0^\infty \Gamma r dr$ is constant, $\Delta r_{\rm I} \sim t^{1/2}$. Conservation of mass then gives $u_{\rm I} \sim \Delta r_{\rm I} t^{-1}$ and hence $u_{\rm I} \sim t^{-(1/2)}$. Since Γh^{-1} is conserved in Lagrangian coordinates (D3), then $h_{\rm I} \sim t^{-1}$. In summary,

$$(u_{\rm I}, h_{\rm I}, \Gamma_{\rm I}, \Delta r_{\rm I}) \sim (t^{-\frac{1}{2}}, t^{-1}, t^{-1}, t^{\frac{1}{2}}),$$
 (3.4)

and

$$(u_{\rm III}, h_{\rm III}, \Delta r_{\rm III}) \sim (t^{-\frac{1}{2}}, 1, t^{\frac{1}{2}}),$$
 (3.5)

with $\Gamma_{\rm III} = 0$.

The summary of the dominant balance in each of the regions is as follows. The balance will be more precisely discussed in the derivation. Region I is where the surfactant concentration is uniform (to leading order), as there are no terms which would balance

the Marangoni stress arising from a non-uniform surfactant concentration. In the IMCE and IMC regimes, the Marangoni stress balances the capillary stress in region II. In the IME regime, the Marangoni stress balances the viscous extensional stress in region II. Inertia does not appear in region II due primarily to the presence of sharp gradients (e.g. the capillary term in (3.1) has third-order spatial derivatives). Region III is where inertia balances capillary stress and/or viscous extensional stress, as there are no surfactants.

3.2. Region I

Expecting a similarity solution, region I is given by $0 \le rt^{-(1/2)} < \eta_f$ for some $\eta_f = \eta_f(\mathcal{M}, Re)$. The similarity coordinate is then given by $\eta := \eta_f^{-1}rt^{-(1/2)} \in [0, 1)$. With the scalings of region I, conservation of momentum (any one of (3.1–3.3)) to leading order gives

$$\frac{\partial \Gamma_{\rm I}}{\partial r} = 0. \tag{3.6}$$

The solution to (3.6), (1.3b) and (1.3c) using global conservation of surfactant $\int_0^\infty \Gamma r dr = 1/2$ shows that

$$u_{\rm I} = \eta_f t^{-\frac{1}{2}} \frac{\eta}{2}, \ h_{\rm I} = \eta_f^{-2} t^{-1} f(\eta), \ \Gamma_{\rm I} = \eta_f^{-2} t^{-1},$$
 (3.7)

where $\eta \in [0, 1)$ and f is given by (using (D4) and (D5))

$$1 = \Gamma_i \left(\left(2 \int_0^{\eta} \eta' f(\eta') d\eta' \right)^{\frac{1}{2}} \right) f(\eta). \tag{3.8}$$

Since f is minimal where Γ_i is maximal (3.8), it then follows that min f = 1 and hence

$$h_{min} = \eta_f^{-2} t^{-1}. (3.9)$$

Finally, in order for the thickness profile $h_{\rm I}$ in region I to match onto region II, $h_{\rm I}$ is singular as the end of region I is approached, $\eta \to 1^-$. By considering the limits $\eta \to 1^-$ of (3.8), it can be shown that $f \sim (1-\eta)^{-1}$ as $\eta \to 1^-$ (see Appendix D.1). Then, $h_{\rm I} \sim t^{-1}(1-\eta)^{-1} = \eta_f t^{-(1/2)}(\eta_f t^{1/2} - r)^{-1}$ as $\eta \to 1^-$.

3.3. Region II

Region II is the transition region between regions I and III, where regularisation of the surfactant front occurs. In order to analyse region II, it is useful to consider the reference frame of the shock propagating at spatial location $r_f = \eta_f t^{1/2}$, with the spatial coordinate given by $\Delta r_{\rm II} := r_{\rm II} - \eta_f t^{1/2}$ and velocity given by $\Delta u_{\rm II} := u_{\rm II} - (1/2)\eta_f t^{-(1/2)}$.

The scalings for region II may be derived as follows. By using conservation of mass and surfactant (1.3b, 1.3c) and matching h (note $h_{\rm I} \sim \eta_f t^{-(1/2)} (\eta_f t^{1/2} - r)^{-1}$ as $r\eta_f^{-1}t^{-(1/2)} \to 1^-$) and Γ onto region I,

$$(\Delta u_{\text{II}}, h_{\text{II}}, \Gamma_{\text{II}}) \sim (\Delta r_{\text{II}} t^{-1}, (\Delta r_{\text{II}})^{-1} t^{-\frac{1}{2}}, t^{-1}).$$
 (3.10)

Then, we may compare the different terms in the momentum balance (3.1–3.3). First, the inertial term has order $O(\Delta u_{\rm II}t^{-1}) \sim (\Delta r_{\rm II})t^{-2} \ll t^{-(3/2)}$ (as $\Delta r_{\rm II}$ is a smaller than $\Delta r_{\rm I} \sim t^{1/2}$), the Marangoni stress term has order $O(\Gamma_{\rm II}(h_{\rm II}\Delta r_{\rm II})^{-1}) \sim t^{-(1/2)}$, the capillary stress term has order $O(h_{\rm II}(\Delta r_{\rm II})^{-3}) \sim (\Delta r_{\rm II})^{-4}t^{-(1/2)}$ and the viscous extensional stress term has order $O(\Delta u_{\rm II}(\Delta r_{\rm II})^{-2}) \sim (\Delta r_{\rm II})^{-1}t^{-1}$. In particular, the inertial term does not appear in region II to leading order.

Then, in the IMC regime, the leading-order momentum balance in region II is between Marangoni and capillary stresses. Hence, the above scalings give $\Delta r_{\rm II} \sim 1$. In the IME regime, the leading-order momentum balance in region II must be between Marangoni and extensional stresses, and hence $\Delta r_{\rm II} \sim t^{-(1/2)}$. Finally, in the IMCE regime, the leading-order momentum balance in region II is between Marangoni and capillary stresses (since balancing Marangoni and extensional stresses gives $\Delta r_{\rm II} \sim t^{-(1/2)}$, which gives the capillary stress term $\sim t^{3/2} \gg t^{-1}$), and hence $\Delta r_{\rm II} \sim 1$. In particular, the long-wavelength approximation will fail to hold for the IME regime as $t \to \infty$ since $\Delta r_{\rm II} \to 0$ (see § 5 for a discussion).

3.3.1. First case (IMCE, IMC regimes): Marangoni–capillary stress balance As above, the scalings discussed for the IMCE and IMC regime are given by

$$(\Delta u_{\rm II}, h_{\rm II}, \Gamma_{\rm II}, \Delta r_{\rm II}) \sim (t^{-1}, t^{-\frac{1}{2}}, t^{-1}, 1).$$
 (3.11)

Then, the momentum balance (3.1) and (3.2) becomes, at leading order,

$$\frac{2}{h_{\rm II}} \frac{\partial \Gamma_{\rm II}}{\partial \Delta r_{\rm II}} = \frac{1}{2\mathcal{M}} \frac{\partial^3 h_{\rm II}}{\partial (\Delta r_{\rm II})^3},\tag{3.12}$$

which integrates with respect to $\Delta r_{\rm II}$ to give

$$\Gamma_{\text{II}} - \eta_f^{-2} t^{-1} = \frac{1}{4\mathcal{M}} \left(h_{\text{II}} \frac{\partial^2 h_{\text{II}}}{\partial (\Delta r_{\text{II}})^2} - \frac{1}{2} \left(\frac{\partial h_{\text{II}}}{\partial \Delta r_{\text{II}}} \right)^2 \right), \tag{3.13}$$

where the spatially constant term $\eta_f^{-2}t^{-1}$ is deduced by matching onto the region I solution (3.7). In particular, since $\Gamma_{\text{III}} = 0$ (region III does not contain surfactants),

$$-\eta_f^{-2} t^{-1} = \lim_{\mathbf{II} \to \mathbf{III}} \frac{1}{4\mathcal{M}} \left(h_{\mathbf{II}} \frac{\partial^2 h_{\mathbf{II}}}{\partial (\Delta r_{\mathbf{II}})^2} - \frac{1}{2} \left(\frac{\partial h_{\mathbf{II}}}{\partial \Delta r_{\mathbf{II}}} \right)^2 \right), \tag{3.14}$$

where $\lim_{I \to III}$ denotes the limit as region III is approached from region II.

3.3.2. Second case (IME regime): Marangoni–extensional stress balance As explained, the scalings in the IME regime are given by

$$(\Delta u_{\text{II}}, h_{\text{II}}, \Gamma_{\text{II}}, \Delta r_{\text{II}}) \sim (t^{-\frac{3}{2}}, 1, t^{-1}, t^{-\frac{1}{2}}).$$
 (3.15)

Then, the momentum balance (3.3) becomes, at leading order,

$$\frac{2}{h_{\rm II}} \frac{\partial \Gamma_{\rm II}}{\partial \Delta r_{\rm II}} = \frac{4}{Re} \left(\frac{\partial^2 \Delta u_{\rm II}}{\partial \Delta r_{\rm II}^2} + \frac{1}{h_{\rm II}} \frac{\partial \Delta u_{\rm II}}{\partial \Delta r_{\rm II}} \frac{\partial h_{\rm II}}{\partial \Delta r_{\rm II}} + \frac{1}{4h_{\rm II}t} \frac{\partial h_{\rm II}}{\partial \Delta r_{\rm II}} \right), \tag{3.16}$$

which integrates with respect to $\Delta r_{\rm II}$ as

$$\Gamma_{\text{II}} - \eta_f^{-2} t^{-1} = \frac{1}{Re} \left(2h_{\text{II}} \frac{\partial \Delta u_{\text{II}}}{\partial \Delta r_{\text{II}}} + \frac{h_{\text{II}}}{2t} \right). \tag{3.17}$$

In particular,

$$-\eta_f^{-2} t^{-1} = \lim_{\Pi \to \Pi I} \frac{1}{Re} \left(2h_{\Pi} \frac{\partial \Delta u_{\Pi}}{\partial \Delta r_{\Pi}} + \frac{h_{\Pi}}{2t} \right), \tag{3.18}$$

where lim_{II→III} denotes the limit as region III is approached from region II.

3.4. Region III

Region III is the region ahead of the front where there is no surfactants and hence $\Gamma=0$. Due to the need to match onto region II, § 3.3, the derivation of the structure of region III also has to consider two different cases. The first case considers the IMCE and IMC regimes, which contain capillary stress terms, where the IMC similarity solutions can directly be seen to be obtainable from the IMCE similarity solutions in the limit $Re\gg 1$. The second case considers the IME regime, which does not contain a capillary stress term; as shown in § 3.3 the absence of these higher derivatives changes the details of region II and hence the matching onto region III. Not containing the curvature gradient term $\partial^3 h/\partial r^3$ also changes the order of the ordinary differential equations (ODEs) of the similarity solutions. Thus, obtaining the IME regime similarity solutions directly from the IMCE similarity solutions is not trivial, but is shown to indeed be the case in § 4.

3.4.1. First case (IMCE, IMC regimes)

The similarity ansatz is given by

$$u_{\text{III}} = \eta_f t^{-\frac{1}{2}} U(\eta), \ h_{\text{III}} = H(\eta),$$
 (3.19)

where $\eta \in (1, \infty)$. Substitution of the self-similarity ansatz (3.19) into the IMCE momentum (3.1) gives

$$-\frac{1}{2}U - \frac{1}{2}\eta \frac{dU}{d\eta} + U \frac{dU}{d\eta} = \frac{1}{2\eta_f^4 \mathcal{M}} \frac{d}{d\eta} \left(\frac{1}{\eta} \frac{d}{d\eta} \left(\eta \frac{dH}{d\eta} \right) \right) + \frac{4}{Re\eta_f^2} \frac{1}{H} \left(\frac{d}{d\eta} \left(\frac{H}{\eta} \frac{d}{d\eta} \left(\eta U \right) \right) - \frac{1}{2} \frac{U}{\eta} \frac{dH}{d\eta} \right).$$
(3.20)

Then, defining $(J, K) := (dH/d\eta, d^2H/d\eta^2)$ and using (1.3b) gives the similarity solutions for the IMCE regime as a system of ODEs for (U, H, J, K)

$$\frac{\mathrm{d}U}{\mathrm{d}\eta} = \left(\frac{\eta}{2} - U\right) \frac{J}{H} - \frac{U}{\eta},\tag{3.21}$$

$$\frac{\mathrm{d}H}{\mathrm{d}\eta} = J,\tag{3.21b}$$

$$\frac{\mathrm{d}J}{\mathrm{d}n} = K,\tag{3.21c}$$

$$\frac{\mathrm{d}K}{\mathrm{d}\eta} = -\frac{K}{\eta} + \frac{J}{\eta^2} + 2\eta_f^4 \mathcal{M} \left(-\frac{U}{2} + \left(U - \frac{\eta}{2} \right) \left(\left(\frac{\eta}{2} - U \right) \frac{J}{H} - \frac{U}{\eta} \right) \right) - \frac{8\eta_f^2 \mathcal{M}}{Re} \left(\left(\frac{1}{2} + \frac{U}{2\eta} - \left(\frac{\eta}{2} - U \right) \frac{J}{H} \right) \frac{J}{H} + \left(\frac{\eta}{2} - U \right) \frac{K}{H} \right), \tag{3.21d}$$

where (3.21*d*) is obtained by repeatedly using (3.21*a*) to eliminate derivatives of *U* in (3.20). By matching onto region II, the behaviour near the left boundary condition at $\eta = 1 + \delta$ for $\delta \ll 1$ can be deduced to satisfy (see Appendix E.1)

$$U(1+\delta) = \frac{1}{2} + \dots, (3.22a)$$

$$H(1+\delta) = \sqrt{8\mathcal{M}}\delta - \frac{\eta_f^2 \mathcal{M}}{Re}\delta^2 \log \delta + q\delta^2 + \dots,$$
 (3.22b)

$$J(1+\delta) = \sqrt{8\mathcal{M}} - \frac{2\eta_f^2 \mathcal{M}}{Re} \delta \log \delta - \frac{\eta_f^2 \mathcal{M}}{Re} \delta + 2q\delta + \dots, \qquad (3.22c)$$

$$K(1+\delta) = -\frac{2\eta_f^2 \mathcal{M}}{Re} \log(\delta) - \frac{3\eta_f^2 \mathcal{M}}{Re} + 2q + \dots,$$
 (3.22d)

for some constant q.

In summary, the similarity solution for region III can be obtained numerically via a shooting algorithm as follows. First, guess some values η_f , q. Then, consider the left boundary condition (3.22) to be at $\eta = 1 + \delta$ for some $\delta \ll 1$ (chosen small enough so that the result is independent of δ). Then, integrate $\eta \to \infty$ subject to (3.21). The process is repeated by adjusting the two constants η_f and q towards satisfying the two constraints

$$H(\infty) = 1 \text{ and } \int_{1}^{\infty} (H - 1)\eta d\eta = \frac{1}{2},$$
 (3.23)

where the second constraint is from global conservation of mass (see Appendix E.1), which shows that the mass that was located in region I at t = 0 must be in region III.

The IMC similarity solutions may be obtained directly from the IMCE similarity solutions in the limit that $Re \gg 1$, thereby omitting the Re^{-1} terms (3.21–3.23); see Appendix F for the exact details.

3.4.2. Second case (IME regime)

The similarity ansatz for the IME regime is still given by (3.19) and when substituted into (3.3) gives

$$-\frac{1}{2}U - \frac{1}{2}\eta \frac{\mathrm{d}U}{\mathrm{d}\eta} + U \frac{\mathrm{d}U}{\mathrm{d}\eta} = \frac{4}{Re\eta_f^2} \frac{1}{H} \left(\frac{d}{\mathrm{d}\eta} \left(\frac{H}{\eta} \frac{d}{\mathrm{d}\eta} \left(\eta U \right) \right) - \frac{1}{2} \frac{U}{\eta} \frac{\mathrm{d}H}{\mathrm{d}\eta} \right). \tag{3.24}$$

Then, letting $J = dH/d\eta$ and using (1.3b) gives the similarity solutions for the IME regime as a system of ODEs for (U, H, J)

$$\frac{\mathrm{d}U}{\mathrm{d}\eta} = \left(\frac{\eta}{2} - U\right) \frac{J}{H} - \frac{U}{\eta},\tag{3.25a}$$

$$\frac{\mathrm{d}H}{\mathrm{d}\eta} = J,\tag{3.25b}$$

$$\frac{\mathrm{d}J}{\mathrm{d}\eta} = \left(\frac{1 + \frac{U}{\eta}}{2\left(U - \frac{1}{2}\eta\right)} + \frac{J}{H}\right)J + \frac{Re\eta_f^2}{4}\left(\frac{HU}{2\left(U - \frac{1}{2}\eta\right)} + \left(U - \frac{\eta}{2}\right)J + \frac{HU}{\eta}\right), \tag{3.25c}$$

where (3.25a) is used repeatedly to eliminate derivatives of U in (3.24). By matching onto region II, the behaviour near the left boundary condition at $\eta = 1 + \delta$ for $\delta \ll 1$ can be deduced to satisfy (see Appendix E.2)

J. Eshima, L. Deike and H.A. Stone

$$U(1+\delta) = \frac{1}{2} - \frac{1}{2}\delta + \dots, \tag{3.26a}$$

$$H(1+\delta) = 2Re\eta_f^{-2} - 4\tilde{q}\delta^{\frac{1}{4}} + \dots,$$
 (3.26b)

$$J(1+\delta) = -\tilde{q}\delta^{-\frac{3}{4}} + \dots, (3.26c)$$

for some constant \tilde{q} to be found. For the IME regime, it is difficult to see from (3.25, 3.26) alone that the IME regime may be recovered upon taking the limit $\mathcal{M} \to \infty$ of the IMCE regime (3.22), which makes sense, given that the regularisation mechanism is fundamentally different in between the IME (§ 3.3.2) and IMCE regimes (§ 3.3.1). However, it is shown in § 4 that the IME regime may in fact be obtained from the IMCE regime in the limit $\mathcal{M} \to \infty$.

In summary, the similarity solution for region III can once again be found via the shooting algorithm, for two parameters η_f , \tilde{q} , with the far-field conditions (3.23).

3.5. Initial surfactant concentration distribution with polynomial decay

In this subsection, we discuss the case where the initial surfactant distribution $\Gamma_i(r) \sim r^{-\alpha}$ as $r \to \infty$. Since the amount of added surfactant is finite, it follows that $\alpha > 2$ (consider $\int_0^\infty r \Gamma_i(r) dr$). The assumption of $\Gamma_i(r)$ decaying faster than polynomial corresponds to $\alpha = \infty$ in the below expressions, which recovers the exact expressions in the rest of the paper. Note that the arguments by Eshima *et al.* (2025) inadvertently had only dealt with the case $\alpha = \infty$.

From (3.7), we have that the thickness in region I is given by $h = \eta_f^{-2} t^{-1} f(\eta)$ with f given by (3.8). Then, $f \sim (1 - \eta)^{-1 - 2(\alpha - 2)^{-1}}$ as $\eta \to 1^-$ (analogous method as in Appendix D). Then, the scaling of region II (3.10) becomes

$$(\Delta u_{\text{II}}, h_{\text{II}}, \Gamma_{\text{II}}) \sim (\Delta r_{\text{II}} t^{-1}, |\Delta r_{\text{II}}|^{-1-2(\alpha-2)^{-1}} t^{-\frac{1}{2}+(\alpha-2)^{-1}}, t^{-1}).$$
 (3.27)

By considering dominant force balance arguments in region II, as in § 3.3, it can be shown that the dominant balance in region II for the IMC and IMCE regimes is still given by Marangoni and capillary stresses with (3.11) modified to

$$(\Delta u_{\rm II}, h_{\rm II}, \Gamma_{\rm II}, \Delta r_{\rm II}) \sim \left(t^{-1+(2\alpha-2)^{-1}}, t^{-\frac{1}{2}+(2\alpha-2)^{-1}}, t^{-1}, t^{(2\alpha-2)^{-1}}\right). \tag{3.28}$$

Similarly, the dominant balance in region II for the IME regime is still given by Marangoni and extensional stresses with (3.15) modified to

$$(\Delta u_{\text{II}}, h_{\text{II}}, \Gamma_{\text{II}}, \Delta r_{\text{II}}) \sim (t^{-\frac{3}{2} + 2\alpha^{-1}}, 1, t^{-1}, t^{-\frac{1}{2} + 2\alpha^{-1}}).$$
 (3.29)

Since the dominant force balance in region II does not change, the solutions shown in the text still follows (see the solution column in table 1).

4. Inertial surfactant deposition with regularisation: verification

In this section, the similarity solutions are verified. First, in § 4.1, the similarity solutions are verified by comparing with the numerical solution of the original thin-film equations in each regime. Then, in § 4.2, it is shown that the self-similarity solutions are self-consistent with each other, in that the IMC and IME similarity solutions agree with the appropriate limits of the IMCE similarity solutions.

4.1. Comparison with numerical solutions of the thin-film equations

In this section, we verify and discuss the similarity solutions obtained in § 3 using the thinfilm equations. The verification is done by checking that the similarity solutions accurately capture the three physical predictions from the thin-film equations in the late-time limit: i) film thinning (t^{-1}) , ii) front propagation $(t^{1/2})$ and iii) capillary wave characteristics.

In figure 8 we compare the IMCE thin-film equations (solid curves) with the similarity solutions (dashed curves), where (a,c,e,g) show the time evolution of the minimum thickness h_{min} and (b,d,f,h) show the time evolution of the location of the surfactant front r_f for $(\mathcal{M},Re)\in\{0.1,1,10\}\times\{1,4,10,40\}$. As previously derived, the similarity solution predicts $h_{min}=\eta_f^{-2}t^{-1}$ and $r_f=\eta_f t^{1/2}$. As expected, for late times, $t\gg 1$, the agreement between the similarity solution and the thin-film equations is good. Similarly, in figure 9 we compare the thickness profile for the thin-film equations at t=1000 (solid curves) with the similarity solutions (dotted curves). The horizontal and vertical axes are given by $rt^{-(1/2)}$ and h. Figure 9(a-l) shows the result of a parameter sweep for $(\mathcal{M},Re)\in\{0.1,1,10\}\times\{1,4,10,40\}$. The agreement between the thin-film equations and the similarity solution is once again robust for the whole parameter space. There are no fitting parameters used in figures 8 and 9 and the similarity solutions therefore capture the desired physical results accurately. The same verification between the thin-film equations and the similarity solutions may be done for the IMC and IME equations and are given in Appendix G.

4.2. Self-consistency of the similarity solutions

We also verify that the IMC and IME regimes are obtained from expected limits of the IMCE regime. Since all three regimes have a front at radial coordinate $r_f(t) = \eta_f t^{1/2}$ as $t \to \infty$, we may compare the value of the prefactor η_f . Figure 10(a) shows $\eta_f(\mathcal{M}, Re)$ as obtained from the similarity solution ODEs in the IMCE regime (see § 3.4.1) versus Re for $\mathcal{M} = 0.1$, 1, 10 (purple, orange, blue–green solid curves) and compares with $\eta_f(\mathcal{M} = 0.1)$, $\eta_f(\mathcal{M} = 1)$, $\eta_f(\mathcal{M} = 10)$ (purple, orange, blue–green dotted lines) as obtained from the similarity solution ODEs in the IMC regime (see Appendix F). Panel (b) shows $\eta_f(\mathcal{M}, Re)$ as obtained from the similarity solution ODEs in the IMCE regime (see § 3.4.1) versus \mathcal{M} for Re = 1, 4, 10 (light grey, grey, dark grey solid curves) and compares with $\eta_f(Re = 1)$, $\eta_f(Re = 4)$, $\eta_f(Re = 10)$ (light grey, grey, dark grey dotted lines) as obtained from the similarity solution ODEs in the IME regime (see § 3.4.2). From figure 10(a), the IMCE regime prediction for η_f agrees well with the IMC regime prediction in the limit $Re \to \infty$; similarly, panel (b) shows that the IMCE regime prediction for η_f agrees well with the IMCE regime prediction in the limit $Re \to \infty$; similarly, panel (b) shows that the IMCE regime prediction for η_f agrees well with the IME regime prediction in the limit $\mathcal{M} \to \infty$. In other words, the relation

$$\lim_{Re \to \infty} \eta_f^{IMCE}(\mathcal{M}, Re) = \eta_f^{IMC}(\mathcal{M}) \text{ and } \lim_{\mathcal{M} \to \infty} \eta_f^{IMCE}(\mathcal{M}, Re) = \eta_f^{IME}(Re)$$
 (4.1)

has been verified (although no formal proof is given).

The late-time similarity solution has been found for inertial surfactant deposition with or without capillary stress and/or extensional stress in the momentum balance, by considering the three possible dynamical regimes IMCE, IMC and IME.

The scalings of the regions I and III away from the surfactant front are the same for all three regimes. However, the details differ in both regions I and III. For the uniform surfactant region I, the value of the coefficient η_f , which sets the location of the surfactant front $(r_f = \eta_f t^{1/2})$ and the minimum thickness $(h_{min} = \eta_f^{-2} t^{-1})$, is dependent on the precise value of \mathcal{M} and Re. For the capillary wave region III, as Re increases, there is less viscous damping of the capillary waves and as \mathcal{M} increases, the thickness profile

J. Eshima, L. Deike and H.A. Stone

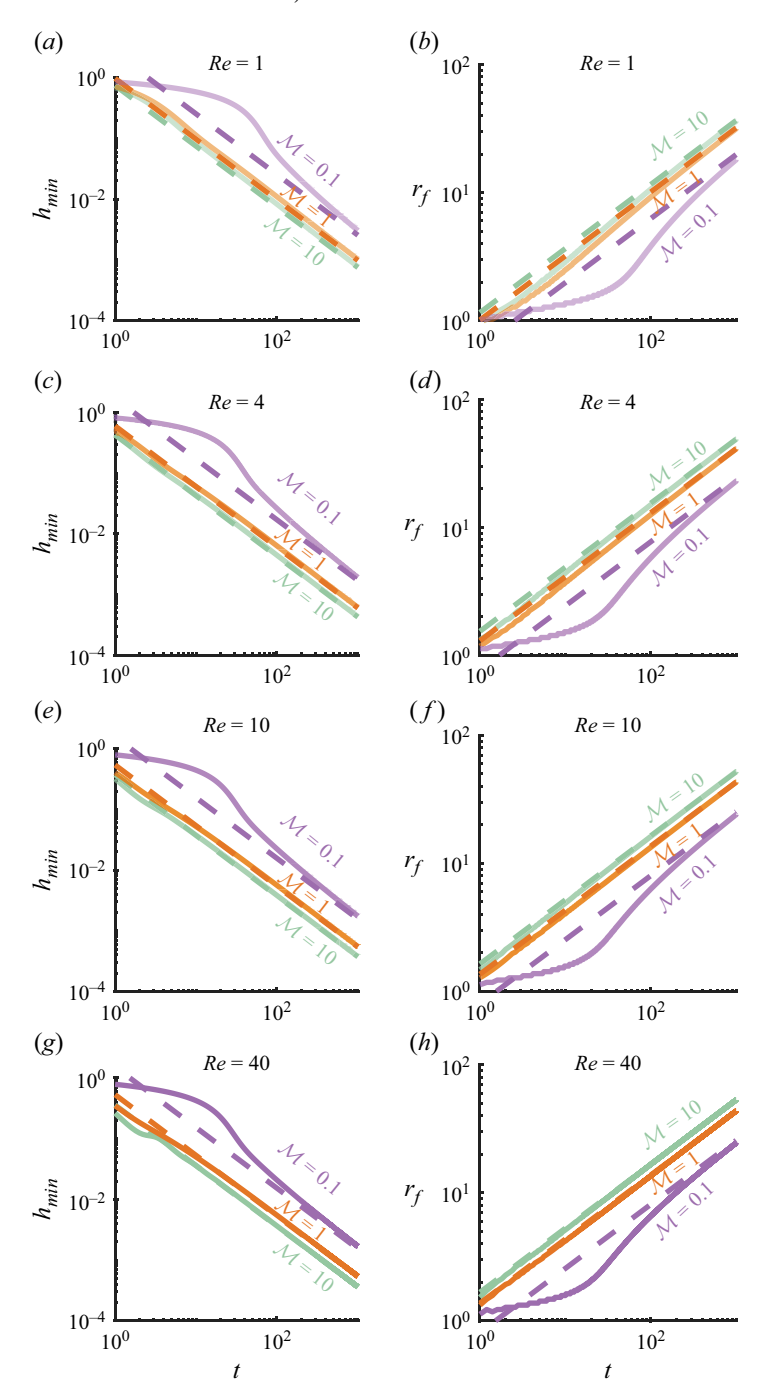


Figure 8. Comparison of the time evolution (a,c,e,g) of the minimum thickness h_{min} and (b,d,f,h) the location of the surfactant front r_f , when comparing the similarity solution (dashed), and the IMCE thin-film equations (solid). For reference, the similarity solution predicts $h_{min} = \eta_f^{-2} t^{-1}$ and $r_f = \eta_f t^{1/2}$. The comparison is obtained for $(\mathcal{M}, Re) \in \{0.1, 1, 10\} \times \{1, 4, 10, 40\}$. The curves are coloured according to $\mathcal{M} = 0.1, 1, 10$ (purple, orange and blue–green, respectively) and shaded according to Re = 1, 4, 10, 40 (light to dark). As expected, for $t \gg 1$, the numerical solutions to the thin-film equation approach the similarity solutions.

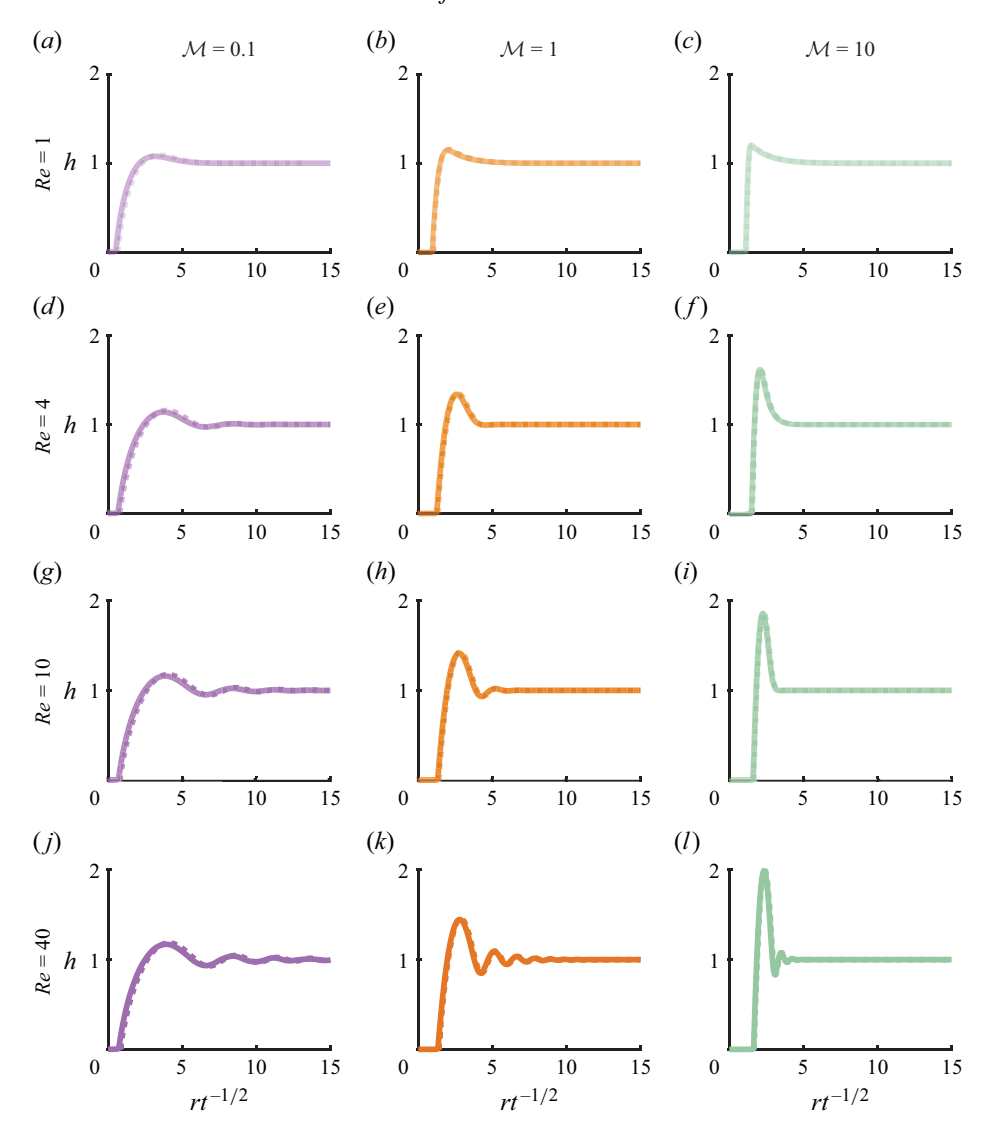


Figure 9. Comparison of the thickness profiles predicted by the thin-film equations at t=1000 (solid curves) and the similarity solutions (dotted curves) for various \mathcal{M} , Re. Thin-film equations are solved for $\Gamma_i = e^{-r^2}$. The horizontal and vertical axes are given by $rt^{-(1/2)}$ and h, where r is the radial coordinate, t is time and h is the thickness. The curves are coloured according to $\mathcal{M} = 0.1$, 1, 10 (purple, orange, blue–green, respectively) and shaded according to Re = 1, 4, 10, 40 (light to dark). (a-l) Parameter sweep for $(\mathcal{M}, Re) \in \{0.1, 1, 10\} \times \{1, 4, 10, 40\}$.

bump becomes sharper, which makes sense since the Marangoni stress is stronger (see figure 9). The IMC regime and IME regime can be obtained as limits of the IMCE regime (§ 4.1).

5. Resolving singularities

The IM and IME regimes have singularities. First, in the IM regime, where there is finitetime shock formation, the front region has width $\sim (t_* - t)^{3/2}$ as $t \to t_*$. The similarity solution for the IME regime can also be considered as shock formation, in the limit as

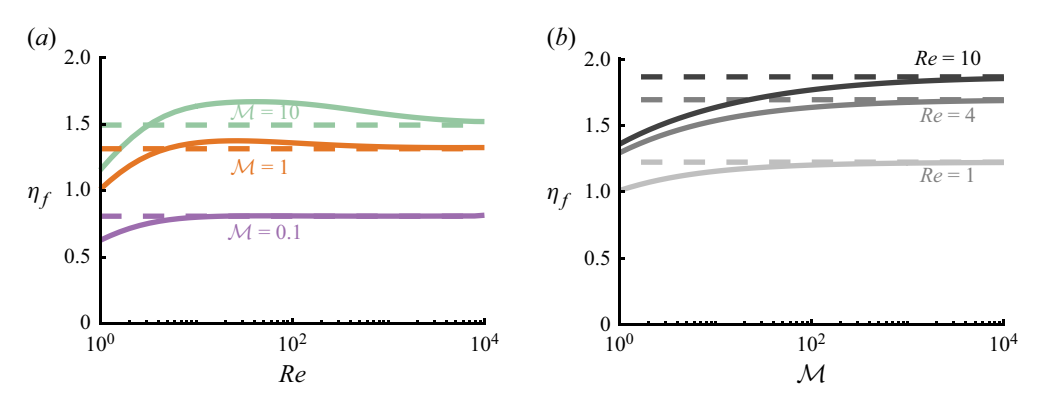


Figure 10. Comparison of IMC and IME regimes as limits of the IMCE regime. (a) Solid curves show $\eta_f(\mathcal{M},Re)$ as obtained from the ODEs found for the similarity solutions in the IMCE regime (see § 3.4.1) against Re for $\mathcal{M}=0.1,1,10$ (purple, orange, blue–green). Dotted lines show $\eta_f(\mathcal{M}=0.1),\eta_f(\mathcal{M}=1),\eta_f(\mathcal{M}=1)$ as obtained from the similarity solution ODEs in the IMC regime (see Appendix F). (b) Solid curves show $\eta_f(\mathcal{M},Re)$ as obtained from the similarity solution ODEs in the IMCE regime against \mathcal{M} for Re=1,4,10 (light grey, grey, dark grey). Dotted lines show $\eta_f(Re=1),\eta_f(Re=4),\eta_f(Re=10)$ (light grey, grey, dark grey) as obtained from the similarity solution ODEs in the IME regime (see § 3.4.2).

 $t \to \infty$, since the front region width $\sim t^{-(1/2)} \to \infty$ as $t \to \infty$. On the other hand, the surfactant front region for the IMC and IMCE regimes have O(1) sized widths at all times. We now discuss two scenarios of how the mathematical singularities in the IM and IME regimes are resolved.

The first scenario is that the flow could no longer be one-dimensional. Recall that, in general, the thin-film expansion for the horizontal velocity follows $u=u_0(r,t)+Re\tilde{\epsilon}^2u_1(r,z,t)+\ldots$ (Chomaz 2001), where u_1 is quadratic in z (i.e. parabolic) and $\tilde{\epsilon}$ is the ratio between the characteristic vertical and horizontal length scales. In the front region for the IM regime, since $\Delta r \sim (t_*-t)^{3/2}$ and $h-h_*\sim (t_*-t)^{1/2}$, the aspect ratio $\tilde{\epsilon}=\epsilon(t_*-t)^{-1}$ (recall the non-dimensionalisation (1.2)). Thus, the parabolic terms can no longer be ignored when $Re(\epsilon(t_*-t)^{-1})^2=O(1)$, i.e. when $t_*-t=O(Re^{1/2}\epsilon)$; note that we only consider $Re\ll\epsilon^{-2}$ and hence $Re^{1/2}\epsilon\ll1$. In the front region for the IME regime, since $\Delta r_{\rm II}\sim t^{-(1/2)}$ and $h_{\rm II}\sim1$, the aspect ratio is $\tilde{\epsilon}=\epsilon t^{1/2}$. Thus, the parabolic terms can no longer be ignored when $Re(\epsilon t^{1/2})^2=O(1)$, i.e. when $t=O(\epsilon^{-2})$, since Re=O(1) in the IME regime.

The second scenario is that the shock is regularised. In the IM regime, although \mathcal{M} , $Re \gg 1$, the capillary term and/or extensional stress terms become important as $t \to t_*^-$. As shown in § 2.2, the shock formation depends on the details of the $O((t_*-t)^{-(1/2)})$ terms in the momentum (2.1). Since $\mathcal{M}^{-1}(\partial^3 h/\partial r^3) \sim \mathcal{M}^{-1}(t_*-t)^{-4}$, and $Re^{-1}(\partial^2 u/\partial r^2) \sim Re^{-1}(t_*-t)^{-(5/2)}$ (when $u-u_*, h-h_* \sim (t_*-t)^{1/2}$ and $\Delta r \sim (t_*-t)^{3/2}$), it then follows that capillary terms can no longer be neglected when $t_*-t=O(\mathcal{M}^{-(2/7)})$ and that extensional stress terms can no longer be neglected when $t_*-t=O(Re^{-(1/2)})$. Similarly, for the infinite-time shock formation in the IME regime, although $\mathcal{M} \gg 1$, the capillary terms eventually become important as $t\to\infty$. As shown in § 3.3.2, the Marangoni stress term $h_{\mathrm{II}}^{-1}(\partial \Gamma_{\mathrm{II}}/\partial \Delta r_{\mathrm{II}}) \sim t^{-(1/2)}$ in the shock region (region II). Since $\mathcal{M}^{-1}(\partial^3 h_{\mathrm{II}}/\partial (\Delta r_{\mathrm{II}})^3) \sim \mathcal{M}^{-1}t^{3/2}$ when $h_{\mathrm{II}} \sim 1$, $\Delta r_{\mathrm{II}} \sim t^{-(1/2)}$, it then follows that the capillary terms can no longer be neglected in the shock region (region II) when $t=O(\mathcal{M}^{1/2})$.

6. Discussion

In this paper, the evolution of the film shape and surfactant distribution in time due to insoluble surfactant deposition on an air-liquid-air thin film in an inertially dominated regime was analysed systematically. First, the similarity solution associated with finite-time shock formation was derived and analysed in § 2 for the IM regime where there are no shock regularisation mechanisms. Allowing for shock regularisation through the inclusion of capillary stress and/or viscous extensional stress (IMCE, IMC, IME regimes) leads to surfactant front propagation and the corresponding late-time similarity solutions were analysed in §§ 3, 4. Finally, in § 5 we discussed ways of resolving the singularities identified in the IM and IME regimes.

It should be noted that the inclusion of extensional stress (IME, IMCE regimes) does not change the previous result by Eshima *et al.* (2025) (for the IMC regime) that the late-time behaviour of the surfactant deposition problem has i) minimum thickness proportional to t^{-1} , ii) surfactant front propagation proportional to $t^{1/2}$ and iii) wave characteristics that can be captured accurately by the relevant similarity solution.

The method of considering eigenvectors and reducing to the Burgers equation in deriving the similarity solution in the IM regime, as shown in § 2.2, is generalisable and will be the subject of a future manuscript.

Out of the IM, IMCE, IMC and IME equations, the most practical set of equations to use is likely the IMCE (1.3), since more physics is accounted for (inertia, Marangoni, capillary, extensional stress). Also, due to the lack of singularities and presence of the extensional stress term, which is dissipative, numerical solutions are comparatively easier to obtain than the IM (singular, no dissipation), IMC (no dissipation) and IME (singular) equations.

There are other mechanisms that could regularise shock fronts due to surfactant deposition, such as the diffusion of surfactants. The inclusion of other physics in the problem set up would also change the deposition dynamics, such as solubility (Bowen & Tilley 2013; Kitavtsev *et al.* 2018; Néel & Villermaux 2018), van der Waals forces (Vaynblat, Lister & Witelski 2001; Wee *et al.* 2022, 2024) and background flow (Burton & Taborek 2007; Fontelos, Kitavtsev & Taranets 2018; Eshima *et al.* 2024).

Supplementary material. Supplementary material is available at https://doi.org/10.1017/jfm.2025.10751.

Acknowledgements. We thank the anonymous reviewers whose suggestions helped to improve the manuscript.

Funding. This work was supported by NSF grants 2242512 and 1844932 to L.D., NSF grant 2127563 to H.A.S. This work used TAMU Faster at Texas A&M High Performance Research Computing through allocation OCE140023 to L.D. from the Advanced Cyberinfrastructure Coordination Ecosystem: Services & Support (ACCESS) program Boerner *et al.* (2023), which is supported by U.S. National Science Foundation grants 2138259, 2138286, 2138307, 2137603 and 2138296.

Declaration of interests. The authors report no conflict of interest.

Appendix A. Derivation of next-order nonlinearity terms in the IM regime

In this appendix, we derive the (2.14). First, (2.10) is expanded to $O(\tau^{\alpha-2})$. Here, it is assumed that $\alpha < 2$, which can be verified a posteriori or alternatively, $\alpha < 2$ can be reasonably justified from numerical data. Then, terms such as h_*u_*/r_* can be neglected. With V defined by (2.12), it follows that

J. Eshima, L. Deike and H.A. Stone

$$\frac{\partial}{\partial \tau} \frac{u'}{V} - \left(u_* + V \frac{u'}{V}\right) \frac{\partial}{\partial r'} \frac{u'}{V} - V \frac{\partial}{\partial r'} \frac{\Gamma'}{\Gamma_*} + \frac{2\frac{d^2\sigma}{d\Gamma^2} (\Gamma_*) \Gamma_*^2}{h_* V} \frac{\Gamma'}{\Gamma_*} \frac{\partial}{\partial r'} \frac{\Gamma'}{\Gamma_*} + V \frac{h'}{h_*} \frac{\partial}{\partial r'} \frac{\Gamma'}{\Gamma_*} = 0, \tag{A1a}$$

$$\frac{\partial}{\partial \tau} \frac{h'}{h_*} - \left(u_* + V \frac{u'}{V} \right) \frac{\partial}{\partial r'} \frac{h'}{h_*} - V \left(1 + \frac{h'}{h_*} \right) \frac{\partial}{\partial r'} \frac{u'}{V} = 0, \tag{A1b}$$

$$\frac{\partial}{\partial \tau} \frac{\Gamma'}{\Gamma_*} - \left(u_* + V \frac{u'}{V} \right) \frac{\partial}{\partial r'} \frac{\Gamma'}{\Gamma_*} - V \left(1 + \frac{\Gamma'}{\Gamma_*} \right) \frac{\partial}{\partial r'} \frac{u'}{V} = 0, \tag{A1c}$$

which gives, upon translating to (\overline{r}, τ) coordinates with $\overline{r} = r' + (u_* + V)\tau$,

$$\begin{split} &\frac{\partial}{\partial \tau} \frac{u'}{V} + V \left(\frac{\partial}{\partial \overline{r}} \frac{u'}{V} - \frac{\partial}{\partial \overline{r}} \frac{\Gamma'}{\Gamma_*} \right) - V \frac{u'}{V} \frac{\partial}{\partial \overline{r}} \frac{u'}{V} \\ &+ \frac{2 \frac{\mathrm{d}^2 \sigma}{\mathrm{d} \Gamma^2} (\Gamma_*) \Gamma_*^2}{h_* V} \frac{\Gamma'}{\Gamma_*} \frac{\partial}{\partial \overline{r}} \frac{\Gamma'}{\Gamma_*} + V \frac{h'}{h_*} \frac{\partial}{\partial \overline{r}} \frac{\Gamma'}{\Gamma_*} = 0, \end{split} \tag{A2a}$$

$$\frac{\partial}{\partial \tau} \frac{h'}{h_*} + V \left(\frac{\partial}{\partial \overline{r}} \frac{h'}{h_*} - \frac{\partial}{\partial \overline{r}} \frac{u'}{V} \right) - V \frac{u'}{V} \frac{\partial}{\partial \overline{r}} \frac{h'}{h_*} - V \frac{h'}{h_*} \frac{\partial}{\partial \overline{r}} \frac{u'}{V} = 0, \tag{A2b}$$

$$\frac{\partial}{\partial \tau} \frac{\Gamma'}{\Gamma_*} + V \left(\frac{\partial}{\partial \overline{r}} \frac{\Gamma'}{\Gamma_*} - \frac{\partial}{\partial \overline{r}} \frac{u'}{V} \right) - V \frac{u'}{V} \frac{\partial}{\partial \overline{r}} \frac{\Gamma'}{\Gamma_*} - V \frac{\Gamma'}{\Gamma_*} \frac{\partial}{\partial \overline{r}} \frac{u'}{V} = 0. \tag{A2c}$$

Then, substituting (2.13), and recalling that without loss of generality $q_3 = -q_1$, we find

$$\frac{\partial \left(A + q_{1}\tau^{\alpha - 1}\right)}{\partial \tau} + V\left(\frac{\partial f_{1}}{\partial \overline{r}} - \frac{\partial f_{3}}{\partial \overline{r}}\right) - V\left(A + q_{1}\tau^{\alpha - 1}\right) \frac{\partial A}{\partial \overline{r}} + \frac{2\frac{d^{2}\sigma}{d\Gamma^{2}}(\Gamma_{*})\Gamma_{*}^{2}}{h_{*}V}\left(A - q_{1}\tau^{\alpha - 1}\right) \frac{\partial A}{\partial \overline{r}} + V\left(A + q_{2}\tau^{\alpha - 1}\right) \frac{\partial A}{\partial \overline{r}} = 0, \tag{A3a}$$

$$\frac{\partial \left(A + q_{2}\tau^{\alpha - 1}\right)}{\partial \tau} + V\left(\frac{\partial f_{2}}{\partial \overline{r}} - \frac{\partial f_{1}}{\partial \overline{r}}\right) - V\left(A + q_{1}\tau^{\alpha - 1}\right) \frac{\partial A}{\partial \overline{r}} - V\left(A + q_{2}\tau^{\alpha - 1}\right) \frac{\partial A}{\partial \overline{r}} = 0, \tag{A3b}$$

$$\frac{\partial \left(A - q_{1}\tau^{\alpha - 1}\right)}{\partial \tau} + V\left(\frac{\partial f_{3}}{\partial \overline{r}} - \frac{\partial f_{1}}{\partial \overline{r}}\right) - V\left(A + q_{1}\tau^{\alpha - 1}\right) \frac{\partial A}{\partial \overline{r}} = 0, \tag{A3c}$$

correct to $O(\tau^{\alpha-2})$ terms. As expected, since we are expanding around an eigenvector of the advection equation, the $O(\tau^{-1})$ terms have vanished (recall that $(\partial A/\partial \overline{r}) = O(\tau^{-1})$). Rearranging (A3) leads to (2.14).

Appendix B. Matching condition for the IM regime

The local singularity region must match onto the region away from the singularity (Eggers & Fontelos 2015). Explicitly, the functions $(u(\bar{r}, \tau), h(\bar{r}, \tau), \Gamma(\bar{r}, \tau))$ must satisfy

$$\lim_{\tau \to 0^+} (u, h, \Gamma)|_{(\Delta, \tau)} = (u, h, \Gamma)|_{(\Delta, 0)}, \tag{B1}$$

for any fixed Δ . From (2.18), we have that $\lim_{\tau \to 0^+} A(\Delta, \tau)$ is bounded, since $F(\eta) \sim \eta^{1/3}$ for $\eta \to \pm \infty$. Thus, (2.13) gives that, for any fixed Δ ,

$$\lim_{\tau \to 0^+} f_i(\Delta, \tau) \text{ is bounded for } i = 1, 2, 3.$$
 (B2)

The matching condition (B2) may be used to eliminate constants. Indeed, eliminating $\partial A/\partial \tau$ via $V^{-1}\times (2.14a)$ –(2.15), integrating with respect to \overline{r} and rearranging gives

$$G(\tau) + c_1 \tau^{\frac{1}{2}} A + c_2 \frac{A^2}{2} + V(f_3 - f_1) = \frac{1}{2} q_1 \overline{\tau} \tau^{-\frac{1}{2}},$$
 (B3)

for some function $G(\tau)$ and constants c_1 , c_2 . Then, for any fixed $\overline{r} = \Delta$, the left-hand side of (B3) is bounded as $\tau \to 0^+$. Thus, we deduce that the constant $q_1 = 0$. The analogous consideration of (2.14b) gives that $q_2 = 0$.

Appendix C. Shock formation along the $u_* - V$ characteristic in the IM regime

In this appendix, the analogue to (2.19) is given for when a shock forms along the $u_* - V$ characteristic instead. Following analogous steps to § 2.2, the similarity solutions for the finite-time singularity is given by

$$u = u_* + V(t_* - t)^{\frac{1}{2}} F\left(\frac{r - r_* + (u_* - V)(t_* - t)}{\left(1 - \frac{\frac{d^2 \sigma}{d\Gamma^2}(\Gamma_*)\Gamma_*^2}{h_* V^2}\right) V(t_* - t)^{\frac{3}{2}}}\right),$$
(C1a)

$$h = h_* - h_*(t_* - t)^{\frac{1}{2}} F\left(\frac{r - r_* + (u_* - V)(t_* - t)}{\left(1 - \frac{\frac{d^2 \sigma}{d\Gamma^2}(\Gamma_*)\Gamma_*^2}{h_* V^2}\right) V(t_* - t)^{\frac{3}{2}}}\right),$$
(C1b)

$$\Gamma = \Gamma_* - \Gamma_*(t_* - t)^{\frac{1}{2}} F\left(\frac{r - r_* + (u_* - V)(t_* - t)}{\left(1 - \frac{\frac{d^2 \sigma}{d\Gamma^2}(\Gamma_*)\Gamma_*^2}{h_* V^2}\right) V(t_* - t)^{\frac{3}{2}}}\right),$$
(C1c)

where F is given by (2.18). Then, the details of shock formation are closely related to the $u_* + V$ characteristic shown in the main text (although with notable sign changes for $h - h_*$ and $\Gamma - \Gamma_*$). In particular, the expressions for max $|\partial u/\partial r|$ and max $|\partial^2 u/\partial r^2|$ are still given by (2.21) and (2.22).

Appendix D. Lagrangian coordinates

In this appendix, the mass and surfactant (1.3b), and (1.3c) are considered in Lagrangian coordinates. Let the Lagrangian coordinate be given by (s, t), where s is the initial material spatial coordinate. We regard the Eulerian spatial coordinate r as a function of s and t, explicitly given by r = r(s, t), where s = r(s, 0). Denote the Lagrangian time derivative by D/Dt. Then, the conservation of mass (1.3b) and surfactant (1.3c) can be written as

$$\left. \frac{Dh}{Dt} \right|_{(s,t)} = \left(-\frac{hu}{r} - h \frac{\partial u}{\partial r} \right) \right|_{r(s,t),t},$$
 (D1)

and

$$\frac{D\Gamma}{Dt}\Big|_{(s,t)} = \left(-\frac{\Gamma u}{r} - \Gamma \frac{\partial u}{\partial r}\right)\Big|_{r(s,t),t}, \tag{D2}$$

which give that

$$\left. \frac{D}{Dt} \left(\frac{\Gamma}{h} \right) \right|_{(s,t)} = 0,\tag{D3}$$

and hence Γ/h is conserved (Chomaz 2001). Since the initial condition (1.5) gives h = 1 and $\Gamma = \Gamma_i(s)$, it then follows for all t that

$$\Gamma(s,t) = \Gamma_i(s)h(s,t),\tag{D4}$$

where global conservation of mass gives s as a function of h,r,t

$$s = \left(2\int_0^r Rh(R, t) dR\right)^{\frac{1}{2}}.$$
 (D5)

D.1. Limit of the thickness profile from region I to region II

In this section, it is shown that the similarity function of the thickness profile $f(\eta)$ (3.7) in region I satisfies $f(\eta) \sim (1-\eta)^{-1}$ as $\eta \to 1^-$. A similar argument was given by Eshima *et al.* (2025), but is reproduced here for completeness. Assume that $f \sim (1-\eta)^{-a}$ as $\eta \to 1^-$ for some a > 0.

Suppose a>1. Then $s=(2\int_0^\eta \eta' f(\eta')\mathrm{d}\eta')^{1/2}$ (from (D5)) satisfies $s\sim (1-\eta)^{(1-a)/2}\to\infty$ as $\eta\to 1^-$. From (3.8), $\Gamma_i(s)=f(\eta)^{-1}\sim (1-\eta)^a\sim s^{2a/(1-a)}$ as $s\to\infty$. This is a contradiction since we consider surfactant distributions $\Gamma_i(r)$ that decay faster than polynomials and hence $a\leqslant 1$. Furthermore, a<1 would imply $s=(2\int_0^\eta \eta' f(\eta')\mathrm{d}\eta')^{1/2}\to \text{constant}$ and hence $f\to \text{constant}$ as $\eta\to 1^-$ by (3.8), which is a contradiction. Thus, a=1.

Appendix E. Derivation of boundary conditions

E.1. The IMCE regime

In this appendix, the boundary conditions at $\eta=1^+$ (3.22) and $\eta=\infty$ (3.23) are derived, valid for the IMCE regime. In the IMCE regime, $h_{\rm II}\sim t^{-(1/2)}$ and hence

$$\lim_{\eta \to 1^+} H = 0. \tag{E1}$$

Also, since $u_{\rm II} = (1/2)\eta_f t^{-(1/2)} + \Delta u_{\rm II}$ where $\Delta u_{\rm II} \sim t^{-1}$, we then have that

$$\lim_{\eta \to 1^+} U = \frac{1}{2}.$$
 (E2)

Then, for $\eta = 1 + \delta$ for $\delta \ll 1$, we may expand as $H(1 + \delta) = H_1 \delta + \ldots$ and $U(1 + \delta) = (1/2) + U_1 \delta + \ldots$. The right-hand side of (3.21*a*) in the limit $\delta \to 0^+$ gives (recall that H' = J)

$$\lim_{\delta \to 0^+} \left(\left(\frac{\eta}{2} - U \right) \frac{J}{H} - \frac{U}{\eta} \right) = -U_1, \tag{E3}$$

and since the limit of the left-hand side of (3.21a) in the limit $\delta \to 0^+$ gives U_1 , it then follows that $U_1 = 0$ and hence

$$\lim_{\eta \to 1^+} \frac{\mathrm{d}U}{\mathrm{d}\eta} = 0. \tag{E4}$$

Also, from the jump condition (3.14), it follows that

$$\lim_{\delta \to 0^+} \frac{1}{4\eta_f^2 \mathcal{M}} \left(H \frac{\mathrm{d}^2 H}{\mathrm{d}\eta^2} - \frac{1}{2} \left(\frac{\mathrm{d}H}{\mathrm{d}\eta} \right)^2 \right) = -\eta_f^{-2},\tag{E5}$$

and hence $(dH/d\eta)|_{\eta=1^+} = J(1^+) = \sqrt{8\mathcal{M}}$. Note that $H(d^2H/d\eta^2)|_{\eta=1^+} = 0$ since otherwise $H(d^3H/d\eta^3)|_{\eta=1^+}$ will be singular, which contradicts (3.21*d*) – see (E7) below. Finally, multiplying (3.21*d*) by *H* and taking the limit $\delta \to 0^+$ gives

$$\lim_{\delta \to 0^+} H \frac{\mathrm{d}K}{\mathrm{d}\eta} = -\lim_{\delta \to 0^+} \frac{8\eta_f^2 \mathcal{M}}{Re} \left(\frac{1}{2} + \frac{U}{2\eta} - \left(\frac{\eta}{2} - U \right) \frac{J}{H} \right) J. \tag{E6}$$

Recalling that $U(1+\delta) = (1/2) + 0\delta + \dots$, $H(1+\delta) = \sqrt{8M\delta} + \dots$, $J = dH/d\eta$ and $K = d^2H/d\eta^2$, it then follows that

$$\lim_{\delta \to 0^+} H \frac{d^3 H}{d\eta^3} = -\frac{2\eta_f^2 \mathcal{M}}{Re} \sqrt{8\mathcal{M}}.$$
 (E7)

Since $H(1+\delta) = \sqrt{8\mathcal{M}}\delta + \dots$, it then follows that

$$\frac{d^3H}{dn^3}(1+\delta) = -\frac{2\eta_f^2\mathcal{M}}{Re}\frac{1}{\delta} + \dots,$$
 (E8)

which can be integrated to give the expansion for $H(1+\delta)$

$$H(1+\delta) = \sqrt{8\mathcal{M}}\delta - \frac{\eta_f^2 \mathcal{M}}{Re}\delta^2 \log \delta + q\delta^2 + \cdots,$$
 (E9)

for some constant q. Note that the equations have two constants η_f , q to be found. Upon differentiating (E9) to obtain $J = dH/d\eta$, $K = d^2H/d\eta^2$, (3.22) follows.

Now, the boundary conditions at $\eta = \infty$ (3.23) are derived. First, $H(\infty) = 1$ follows from the film being undisturbed at the far field. In order to show that $\int_1^\infty (H-1)\eta d\eta = (1/2)$, one can consider the integral $I_m(t) := \int_0^\infty (h-1)r dr$, which can be thought of as the total excess mass with respect to the flat film. Since there are diffusion terms (viscous dissipation), h decays to 1 much faster than polynomials with exponential decay as $r \to \infty$ for any t. Mathematically, such a decay can be seen directly from considering the large η behaviour of (3.21). Then, we can integrate $I_m(t)$ under the integral sign, to obtain

$$I'_{m}(t) = \int_{0}^{\infty} \frac{\partial h}{\partial t} r dr = -\int_{0}^{\infty} \frac{\partial}{\partial r} (ruh) dr = -[ruh]_{0}^{\infty} = 0,$$
 (E10)

which gives that $I_m(t)$ is conserved. Since $I_m(0)=0$, it then follows that $I_m(t)=0$ for all t. Finally, $h_{\rm I}\sim t^{-1}$ as $t\to\infty$ and hence $\int_0^{\eta_f t^{1/2}} (h-1)r{\rm d} r=-(1/2)\eta_f^2 t+O(1)$. Then, since $I_m(t)=0$, $\int_{\eta_f t^{1/2}}^{\infty} (h-1)r{\rm d} r=(1/2)\eta_f^2 t+O(1)$ as $t\to\infty$, which gives

$$\int_{1}^{\infty} (H-1) \eta \mathrm{d}\eta = \frac{1}{2}.$$
 (E11)

It should be noted that (E11) implies $H(\infty) = 1$, but importantly $H(\infty) = 1$ does not imply (E11). For the shooting algorithm, a given guess of η_f will have an associated q such that $H(\infty) = 1$. The choice of η_f is adjusted until (E11) is satisfied.

E.2. The IME regime

In the IME regime, since $u_{\rm II} = (1/2)\eta_f t^{-(1/2)} + \Delta u_{\rm II}$ with $\Delta u_{\rm II} \sim t^{-(3/2)}$ and (3.18), the functions $U(\eta)$ and $H(\eta)$ satisfy

$$\lim_{\eta \to 1^+} U = \frac{1}{2},\tag{E12}$$

and

$$\lim_{\eta \to 1^+} H\left(2\frac{\mathrm{d}U}{\mathrm{d}\eta} + \frac{1}{2}\right) = -Re\eta_f^{-2}. \tag{E13}$$

In particular, (E13) gives that $H(1^+)$ is finite since numerical data of the thin-film equation solution show $2(dU/d\eta)|_{\eta=1^+} + (1/2)$ clearly bounded away from 0. Also,

$$\lim_{\eta \to 1^+} \left(\frac{J}{H} \left(\frac{\eta}{2} - U \right) \right) = 0, \tag{E14}$$

since $((\eta/2) - U) = O(\delta)$ for $\eta = 1 + \delta$ and J is a term much smaller than $O(\delta^{-1})$ since H is finite at $\eta = 1^+$. Then, (E12), (E14) and (3.25a) give

$$\lim_{\eta \to 1^{+}} \frac{dU}{d\eta} = -\frac{1}{2},\tag{E15}$$

which substituted into (E13) gives

$$\lim_{n \to 1^{+}} H = 2Re\eta_f^{-2}.$$
 (E16)

If one naively assumes that $J(1^+)$ is also finite, then expanding (3.25c) for $\eta=1+\delta$ for $\delta\ll 1$ gives that $(\mathrm{d}J/\mathrm{d}\eta)|_{1+\delta}=-((3/4)J(1)+(1/8)Re^2)\delta^{-1}+\dots$ and the only self-consistent conclusion is that $J(1)=-(1/6)Re^2$. Such a conclusion can be seen to be wrong from numerical data, which suggest that $J(1^+)$ is bounded away from $-(1/6)Re^2$. More rigorously, the forcing of J(1) to be a particular value means that the system is overdetermined, where there is one free variable η_f to satisfy two conditions (3.23). Then, $J(1^+)$ is not finite. In particular, the thickness profile H has a cusp at the left boundary $\eta=1$.

With the understanding that $J(1^+)$ is not finite, one may expand $\eta = 1 + \delta$ for $\delta \ll 1$ where (3.25c) gives $(dJ/d\eta) \approx -(3/4)\delta^{-1}J$ and hence $J = -\tilde{q}\delta^{-(3/4)}$ to leading order for some constant \tilde{q} to be found. In summary, (3.26) is obtained.

The boundary conditions at $\eta = \infty$ are identical to the IMCE regime and the derivation is also identical.

Appendix F. The IMC regime in region III

The similarity solution for region III may be just derived from the IMCE equations upon letting $Re \gg 1$ and hence ignoring Re^{-1} terms in (3.21–3.23). However, the resulting IMC similarity solutions may be exactly integrated once to form a more simple set of equations.

The integration may be done as follows. From (3.21) in the limit $Re \gg 1$ (or from the similarity ansatz (3.19) substituted into (3.2))

$$-\frac{1}{2}U - \frac{1}{2}\eta \frac{\mathrm{d}U}{\mathrm{d}\eta} + U \frac{\mathrm{d}U}{\mathrm{d}\eta} = \frac{1}{2\eta_f^4 \mathcal{M}} \frac{d}{\mathrm{d}\eta} \left(\frac{1}{\eta} \frac{d}{\mathrm{d}\eta} \left(\eta \frac{\mathrm{d}H}{\mathrm{d}\eta} \right) \right). \tag{F1}$$

In particular, (F1) may be integrated once to give

$$c - \frac{1}{2}\eta U + \frac{1}{2}U^2 = \frac{1}{2\eta_f^4 \mathcal{M}} \left(\frac{1}{\eta} \frac{d}{d\eta} \left(\eta \frac{dH}{d\eta} \right) \right), \tag{F2}$$

for some constant c. In fact, it can be shown that c=0 (Eshima $et\ al.\ 2025$) by rewriting (F2) in the form $c\eta^{-1}=\cdots$ and using that $\int_1^\infty c\eta^{-1}\mathrm{d}\eta$ is bounded if and only if c=0. Then, letting $J=\mathrm{d}H/\mathrm{d}\eta$ and using (1.3b) again, the similarity solutions for the IMC regime can be given as a system of ODEs for (U,H,J)

$$\frac{\mathrm{d}U}{\mathrm{d}\eta} = -\frac{UJ}{H} - \frac{U}{\eta} + \frac{J\eta}{2H},\tag{F3a}$$

$$\frac{\mathrm{d}H}{\mathrm{d}\eta} = J,\tag{F3b}$$

$$\frac{\mathrm{d}J}{\mathrm{d}\eta} = -\frac{J}{\eta} + \eta_f^4 \mathcal{M} \left(U^2 - \eta U \right). \tag{F3c}$$

From (3.22), in the limit $Re \gg 1$, the left boundary condition at $\eta = 1 + \delta$ for $\delta \ll 1$ can be deduced to satisfy

$$U(1+\delta) = \frac{1}{2} + \dots, \tag{F4a}$$

$$H(1+\delta) = \sqrt{8\mathcal{M}}\delta + \dots, \tag{F4b}$$

$$J(1+\delta) = \sqrt{8\mathcal{M}} + \dots$$
 (F4c)

Note that (F4) can also be deduced directly from noting that $u_{\rm II} = (1/2)\eta_f t^{-(1/2)} + \Delta u_{\rm II}$ where $\Delta u_{\rm II} \sim t^{-1}$, $h_{\rm II} \sim t^{-(1/2)}$ and (3.14).

Again, the similarity solution for region III can be obtained using a shooting algorithm. A key difference to the IMCE regime is that there is only one shooting parameter, η_f , which makes sense, given that the similarity solutions were already integrated once (see (F2)). Thus, the correct η_f can be found by adjusting the constraint towards satisfying

$$H(\infty) = 1. (F5)$$

Appendix G. Additional verification plots of the late-time similarity solution

The appendix contains the verification between the thin-film equations and the similarity solutions, that was omitted for brevity.

Figure 11, reproduced from Eshima *et al.* (2025), compares the thin-film equations (solid) with the similarity solution prediction (dotted), where (a) verifies the minimum thickness h_{min} , (d) verifies the location of the surfactant front r_f and (b,c,e) verify the capillary wave characteristics. Again, there are no fitting parameters and the similarity solution is therefore verified.

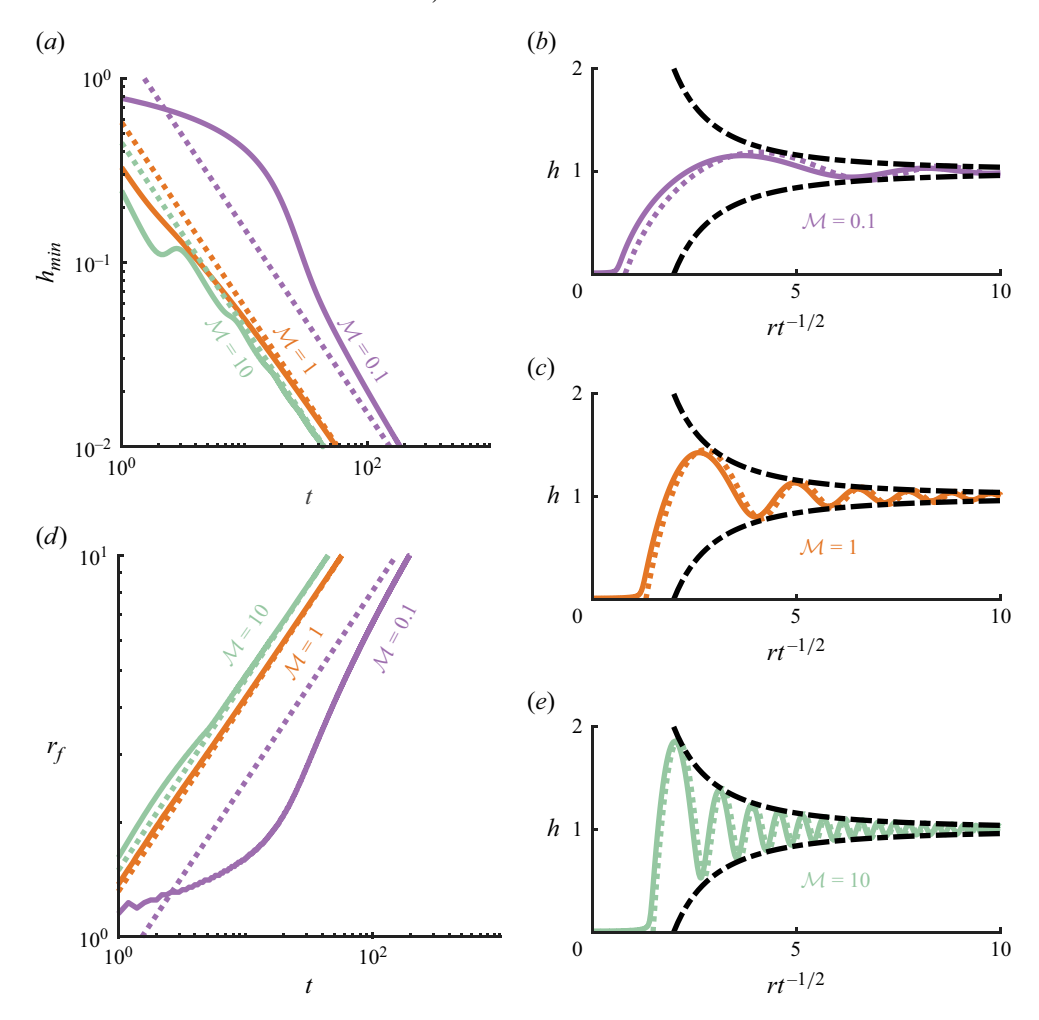


Figure 11. Verification of the similarity solution (dotted) using the thin-film equations (solid) (3.2), (1.3b), (1.3c) in the IMC regime. Thin-film equations are solved for $\Gamma_i = e^{-r^2}$. (a) Minimum thickness h_{min} is compared for $\mathcal{M} = 0.1$, 1, 10 (purple, orange, blue–green, respectively). (d) Surfactant front r_f is compared for $\mathcal{M} = 0.1$, 1, 10 (purple, orange, blue–green, respectively). (b,c,e) Thickness h profiles compared for $\mathcal{M} = 0.1$, 1, 10 (purple, orange, blue–green, respectively), where thin-film equation profiles are chosen at suitable late times (explicitly, at t = 186, 56, 44, when $h_{min} \approx 0.01$). The expressions for the envelope $h = 1 \pm 4tr^{-2}$ (dash-dotted curves) are also included in (b,c,e) – see Eshima et al. (2025) for the derivation. Reprinted with permission from Eshima et al. (2025) (their figure 3, reformatted and adapted to use the label \mathcal{M} , instead of $B = \mathcal{M}^{-1}$). Copyright (2025) by the American Physical Society. https://doi.org/10.1103/PhysRevLett.134.214002.

As expected, the thickness profiles in the IMC regime (figure 11b,c,e) look similar to the thickness profile in the IMCE regime (figure 9) as Re increases, although even the Re = 40 case for the IMCE regime (figure 9j,k,l) shows noticeable viscous damping effects of the capillary waves in comparison with the IMC regime.

G.2. The IME regime

Figure 12 is the analogue to figure 11 for the IME regime and therefore verifies the similarity solution. Again, as expected, the IME regime thickness profiles look similar to the IMCE regime thickness profiles as $\mathcal{M} \to \infty$.

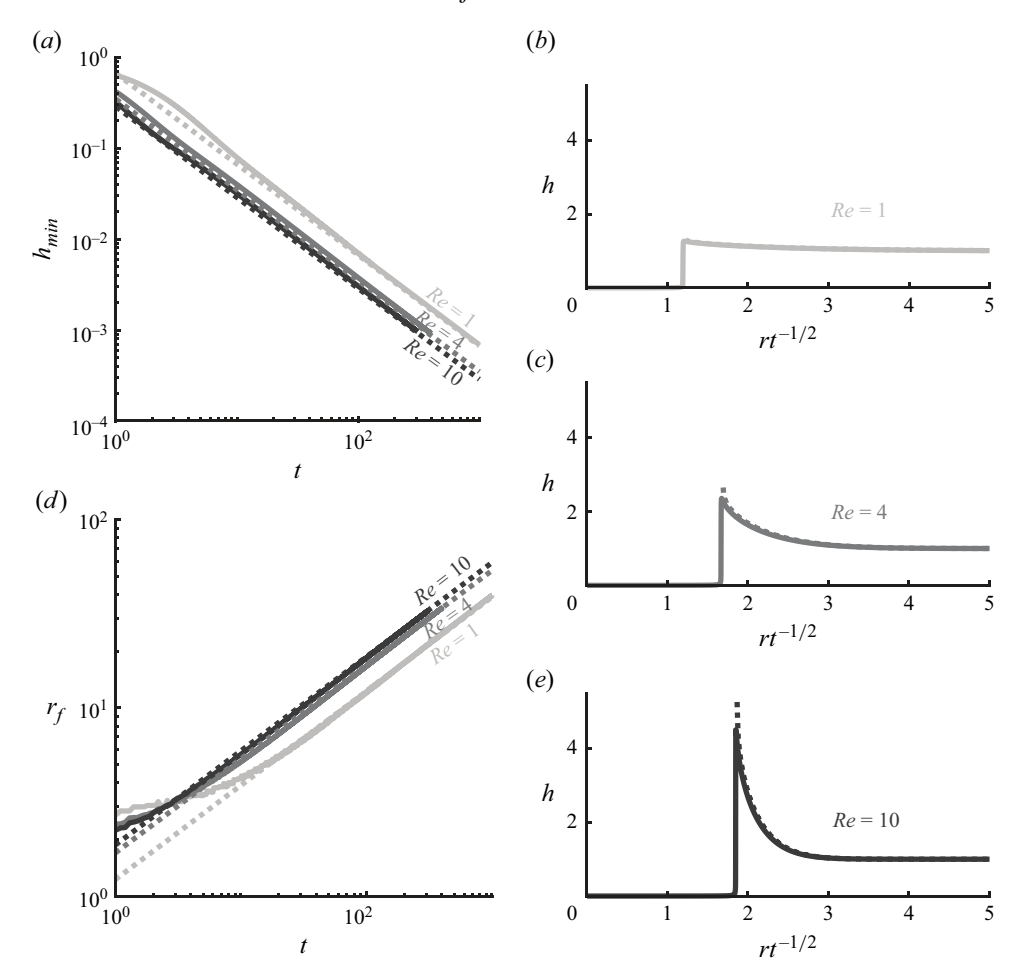


Figure 12. Verification of the similarity solution (dotted) using the thin-film equations (solid) (3.3), (1.3b), (1.3c). The thin-film equations are solved for $\Gamma_i = e^{-r^2}$. (a) Minimum thickness h_{min} is compared for Re = 1, 4, 10 (light grey, grey, dark grey, respectively). (b,c,e) Thickness h profiles compared for Re = 1, 4, 10 (light grey, grey, dark grey, respectively), where thin-film equation profiles are chosen at suitable late times (t = 710, 370, 300, respectively, where $h_{min} \approx 0.001$).

REFERENCES

BOERNER, T.J., DEEMS, S., FURLANI, T.R., KNUTH, S.L. & TOWNS, J. 2023 Access: advancing innovation: NSF's advanced cyberinfrastructure coordination ecosystem: services & support. In *Practice and Experience in Advanced Research Computing 2023: Computing for the Common Good*, pp. 173–176. Association for Computing Machinery.

BOUROUIBA, L. 2021 The fluid dynamics of disease transmission. *Annu. Rev. Fluid Mech.* **53**, 473–508. BOWEN, M. & TILLEY, B.S. 2013 On self-similar thermal rupture of thin liquid sheets. *Phys. Fluids* **25** (10), 102105.

Brenner, M.P. & Gueyffier, D. 1999 On the bursting of viscous films. *Phys. Fluids* 11 (3), 737–739.

BREWARD, C.J. W. 1999 The mathematics of foam. PhD thesis, Oxford University, Oxford, UK.

Burton, J.C. & Taborek, P. 2007 Two-dimensional inviscid pinch-off: an example of self-similarity of the second kind. *Phys. Fluids* **19** (10), 102109.

CHOMAZ, J.-M. 2001 The dynamics of a viscous soap film with soluble surfactant. *J. Fluid Mech.* 442, 387–409.

CRAMERI, F. 2021 Scientific colour maps (7.0.1). Zenodo. https://doi.org/10.5281/zenodo.5501399.

J. Eshima, L. Deike and H.A. Stone

- DE WIT, A., GALLEZ, D. & CHRISTOV, C.I. 1994 Nonlinear evolution equations for thin liquid films with insoluble surfactants. *Phys. Fluids* 6 (10), 3256–3266.
- DEIKE, L. 2022 Mass transfer at the ocean–atmosphere interface: the role of wave breaking, droplets, and bubbles. *Annu. Rev. Fluid Mech.* **54**, 191–224.
- EGGERS, J. & FONTELOS, M.A. 2009 The role of self-similarity in singularities of partial differential equations. *Nonlinearity* 22 (1), R1.
- EGGERS, J. & FONTELOS, M.A. 2015 Singularities: Formation, Structure, and Propagation. Cambridge University Press.
- ERNEUX, T. & DAVIS, S.H. 1993 Nonlinear rupture of free films. *Phys. Fluids A: Fluid Dyn.* **5** (5), 1117–1122. ESHIMA, J., DEIKE, L. & STONE, H.A. 2024 Thin-film flow due to an asymmetric distribution of surface tension and applications to surfactant deposition. *J. Fluid Mech.* **992**, A2.
- ESHIMA, J., STONE, H.A. & DEIKE, L. 2025 Precursors of thin film rupture: similarity solution of surfactant-driven, inertial capillary waves. *Phys. Rev. Lett.* **134** (21), 214002.
- FONTELOS, M.A., KITAVTSEV, G. & TARANETS, R.M. 2018 Asymptotic decay and non-rupture of viscous sheets. Z. Angew. Math. Phys. 69, 1–21.
- VAN HOOFT, J.A., POPINET, S., VAN HEERWAARDEN, C.C., VAN DER LINDEN, S.J.A., DE ROODE, S.R. & VAN DE WIEL, B.J.H. 2018 Towards adaptive grids for atmospheric boundary-layer simulations. *Boundary-Layer Meteorol.* 167, 421–443.
- HOWELL, P.D. 1996 Models for thin viscous sheets. Eur. J. Appl. Maths 7 (4), 321–343.
- JENSEN, O.E. & GROTBERG, J.B. 1992 Insoluble surfactant spreading on a thin viscous film: shock evolution and film rupture. *J. Fluid Mech.* **240**, 259–288.
- KITAVTSEV, G., FONTELOS, M.A. & EGGERS, J. 2018 Thermal rupture of a free liquid sheet. *J. Fluid Mech.* **840**, 555–578.
- MANIKANTAN, H. & SQUIRES, T.M. 2020 Surfactant dynamics: hidden variables controlling fluid flows. J. Fluid Mech. 892, P1.
- NÉEL, B. & VILLERMAUX, E. 2018 The spontaneous puncture of thick liquid films. J. Fluid Mech. 838, 192–221.
- Oron, A., Davis, S.H. & Bankoff, S.G. 1997 Long-scale evolution of thin liquid films. *Rev. Mod. Phys.* 69 (3), 931.
- POMEAU, Y., LE BERRE, M., GUYENNE, P. & GRILLI, S. 2008 Wave-breaking and generic singularities of nonlinear hyperbolic equations. *Nonlinearity* 21 (5), T61.
- POPINET, S. & collaborators 2013–2025 Basilisk, http://basilisk.fr.
- POULAIN, S., VILLERMAUX, E. & BOUROUIBA, L. 2018 Ageing and burst of surface bubbles. *J. Fluid Mech.* **851**, 636–671.
- SAVVA, N. & BUSH, J.W.M. 2009 Viscous sheet retraction. J. Fluid Mech. 626, 211-240.
- VAYNBLAT, D., LISTER, J.R. & WITELSKI, T.P. 2001 Rupture of thin viscous films by van der Waals forces: evolution and self-similarity. *Phys. Fluids* 13 (5), 1130–1140.
- VERON, F. 2015 Ocean spray. Annu. Rev. Fluid Mech. 47, 507-538.
- WEE, H., KUMAR, A.H., LIU, X. & BASARAN, O.A. 2024 Escape from pinch-off during contraction of liquid sheets and two-dimensional drops of low-viscosity fluids. *Phys. Rev. Fluids* 9 (10), 103601.
- WEE, H., WAGONER, B.W. & BASARAN, O.A. 2022 Spontaneous rupture of surfactant-covered thin liquid sheets. *Phys. Rev. Fluids* 7 (9), 094005.